

# Physical confinement selectively favours bacterial growth based on cell shape

M Sreepadmanabh<sup>1</sup>, Meenakshi Ganesh<sup>1,2</sup>, Pratibha Sanjenbam<sup>1</sup>, Christina Kurzthaler<sup>3</sup>, Deepa Agashe<sup>1</sup>, and Tapomoy Bhattacharjee<sup>1\*</sup>

<sup>1</sup>National Centre for Biological Sciences, Tata Institute of Fundamental Research, Bangalore

<sup>2</sup>Indian Institute of Science Education and Research, Mohali

<sup>3</sup>Max Planck Institute for the Physics of Complex Systems, Dresden

\*email: [tapa@ncbs.res.in](mailto:tapa@ncbs.res.in)

## Abstract

How are bacterial communities altered by changes in their microenvironment? Evidence from homogeneous liquid or flat plate cultures implicates biochemical cues — such as variation in nutrient composition <sup>1,2</sup>, response to chemoattractants and toxins <sup>3,4</sup>, and inter-species signalling <sup>5,6</sup> — as the primary modes of bacterial interaction with their microenvironment. However, these systems fail to capture the effect of physical confinement on bacteria in their natural habitats. Bacterial niches like the pores of soil, mucus, and infected tissues are disordered microenvironments with material properties defined by their internal pore sizes and shear moduli<sup>7–11</sup>. Here, using three-dimensional matrices that match the viscoelastic properties of gut mucus, we test how altering the physical properties of their microenvironment influences bacterial growth under confinement. We find that low aspect-ratio bacteria form compact, spherical colonies under confinement while high aspect-ratio bacteria push their progenies further outwards to create elongated colonies with a higher surface area, enabling increased access to nutrients. As a result, the population level growth of high aspect-ratio bacteria is more robust to increased physical confinement compared to that of low aspect-ratio bacteria. Thus, our results capture experimental evidence showing that physical constraints can play a selective role in bacterial growth based on cell shape.

## 1. Introduction

Most natural habitats host diverse bacterial communities, which actively respond to extrinsic environmental cues that reflect the dynamic properties of their microenvironments <sup>7,12</sup>. Identifying the basis of these feedback-response cycles is critical for describing the evolution of natural microbial populations, characterizing host-symbiont crosstalk and interdependency, as well as understanding pathogenesis to design effective antibiotics. A major class of such interactions is understood within the framework of biochemical signalling, where small molecules (such as metabolites, growth factors, antibiotics, and chemoattractants) drive cellular perception and consequent responses <sup>1–4</sup>. These processes also directly impact the composition of natural microbial communities, wherein co-existing species exhibit symbiotic, mutualistic, or predatory interactions with each other <sup>5,6</sup>. However, current experimental approaches designed to explore such interactions rely on bacteria cultured in homogeneous liquid broths or on surfaces of 2D flat plates, which do not capture the structural complexity of many natural niches. Bacteria often reside in complex and disordered 3D microenvironments like soil, inter-tissue pores, and biological hydrogels such as mucus, which feature a wide range of material properties <sup>9,13,14</sup>. For example, the porosity and stiffness of soil is affected by its moisture content and granularity <sup>15</sup>. The spatial architecture of tissues also undergoes significant structural alterations as a result of ECM

(extracellular matrix) deposition and enzymatic remodelling by fibroblasts and immune cells<sup>16</sup>. Similarly, the viscoelastic properties of mucus vary with diet, inflammatory responses, microbial enzymatic activity, and pathologies like cystic fibrosis<sup>8,17,18</sup> (**Fig. 1a**). Furthermore, bacterial colonies physically constrained within these complex 3D matrices experience diffusion-limited growth<sup>19,20</sup>. In contrast, bacteria growing in homogeneously well-mixed liquid cultures have unrestricted access to nutrients, while colonies on a flat agar surface receive oxygen supply from the top as well as direct nutrient access from the underlying substratum. While diffusion-limited zones can be established during growth over time, these usually affect the colony's core once multilayer 3D growth occurs, with cells piling on top of each other<sup>21</sup>. However, growth under 3D confinement could introduce such consumption-diffusion limited zones locally around small single cell-derived colonies, despite there being a global abundance of the nutrients in the bulk medium. Hence, growth under 3D becomes fundamentally different from that on standard 2D interfaces. Previous work has investigated colony growth under nutrient-replete 2D conditions, extending growth-generated stresses as a putative mechanism for achieving quasi-3D conformations<sup>22,23</sup>. However, these studies do not fully capture bacterial growth in disordered, confined microenvironments. Growing evidence indicates that bacterial motility is significantly altered by confinement within a granular and porous matrix<sup>24</sup> and the growth of initially smooth, densely-packed bacterial populations under 3D confinement shows generic surface roughening morphodynamics driven by differential nutrient accessibility<sup>20</sup>. Despite this, bacterial population level growth and colony organization under complex and disordered confinement remains insufficiently described. Consequently, whether and how the physical constraints imposed by a 3D growth microenvironment influence microbial populations remains unclear.

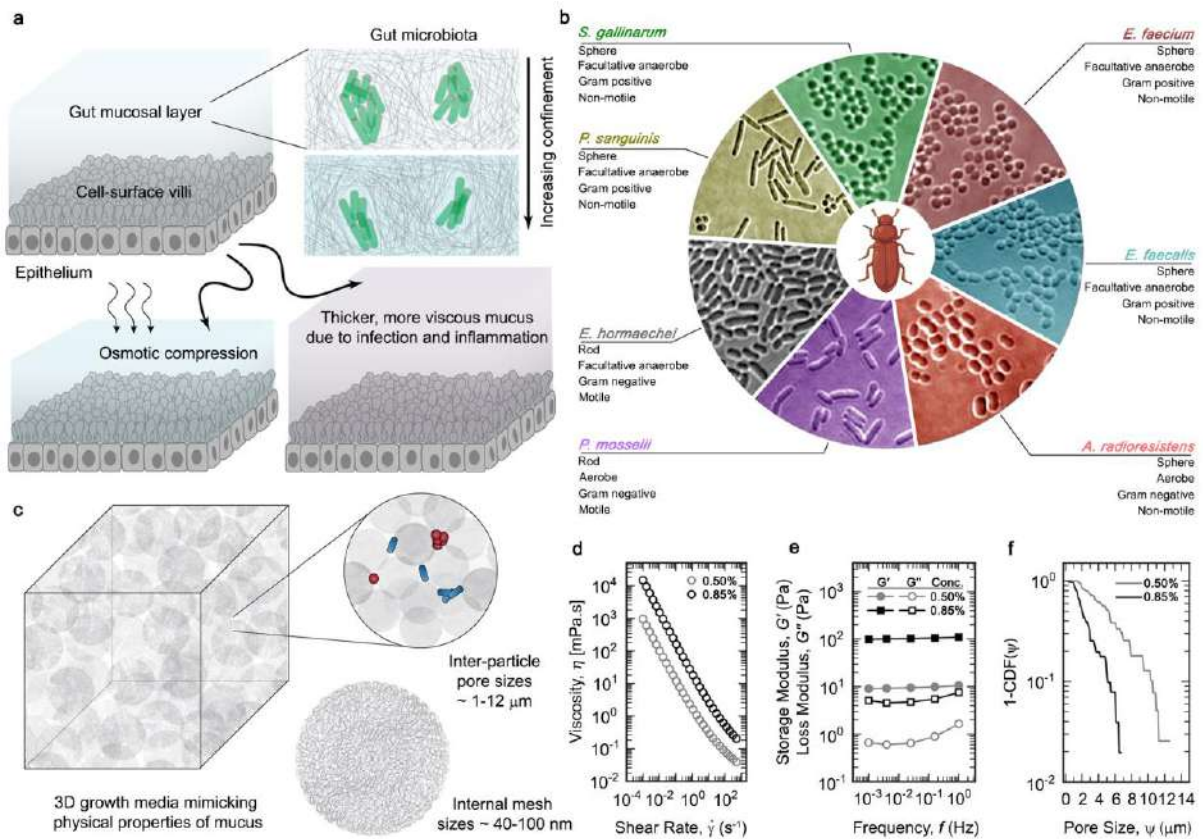


**Figure 1: An *in vitro* 3D growth matrix with tunable viscoelastic properties.** (a) The physical properties of the mucosal layer are diverse and are altered by factors such as a change in diet, infection, inflammation, and enzymatic degradation of fibers by microbes. (b) Different gut-derived microbial strains from red flour beetles, imaged in brightfield (pseudo-colored for enhanced contrast). (c) By packing highly swollen polymeric hydrogel granules at jamming concentrations, we design an *in vitro* 3D growth medium, which provides a granular and internally porous microenvironment for bacterial growth under confinement. (d-f) The physical properties of the microgel growth medium are highly tunable based on the mass percentage of hydrogel granules relative to liquid LB (%weight/volume). Here, we show both soft and low confinement (0.50%) as well as stiff and high confinement (0.85%) matrices, the viscoelastic properties of which approximately match mucosal samples from natural sources<sup>26</sup>. Rheological measurements shown here either apply a unidirectional shear at different rates to measure the viscosity, or, a small amplitude (1%) of oscillatory strain at different frequencies to measure the shear moduli of the 3D growth media. The storage modulus ( $G'$ ) is a measure of the elastic solid-like nature, while the loss modulus ( $G''$ ) signifies the viscous properties of the material. The porosity of the medium, shown here as a complementary cumulative distribution function (1-CDF) of all the inter-particle pore spaces, determines the degree of confinement, and can be tuned by altering the packing fraction of the hydrogel granules.

In this work, we present experimental evidence for confinement-dependent growth dynamics that selectively favour specific bacterial morphologies. We prepare transparent, granular 3D growth media—a special type of porous matrix for direct measurement of bacterial growth as well as visualization of colony organisation under different biomimetic degrees of confinement—that broadly mimic the structural and viscoelastic properties of mucus, a biological hydrogel. Using several different bacterial strains isolated from the gut mucus of red flour beetles we show how an increase in confinement confers a growth advantage to bacteria with a higher aspect ratio. Our study combines quantitative measurements of bacterial growth and colony morphology, agent-based modelling, numerical calculations, as well as *in vitro* co-

1 culture experiments, to establish a generalized principle for growth under confinement. By  
2 experimentally manipulating cellular morphology, we also demonstrate a remarkable  
3 interconvertible behaviour between high and low aspect ratio forms of the same bacterial  
4 species, which strongly implicates single-cell morphology as a broad determinant of colony  
5 architecture and growth success under physical confinement. Importantly, we show that  
6 population-level variation in growth dynamics can arise without invoking mechanisms such as  
7 genetic mutations, behavioural differences, or cellular responses to biochemical cues. Rather,  
8 our work suggests that the composition of heterogeneous microbial populations may be  
9 strongly dependent on efficient colony organization under increased confinement that  
10 selectively favours bacterial species with a high aspect ratio morphology. These principles are  
11 valuable for the experimental elucidation and theoretical modelling of microbial dynamics in  
12 complex, spatiotemporally varying natural niches.

## 2. Objectives

In this work, we derive inspiration from outstanding questions in microbiological research and industrial biotechnology. We have known about bacteria for well over three hundred years. When Leeuwenhoek observed the very first figments of microbial life, he did so from samples gathered from natural settings such as soil, blood, tissues, and plants – all of which are complex 3D materials. However, our overt reliance on homogeneous liquid broths and flat 2D agar plates over the years has severely constrained our ability to fully understand the bacterial growth dynamics in physiologically relevant scenarios.

This has critical relevance not just for advancing fundamental biology, but also from a translational perspective. Effective design of antimicrobial drugs and their high-throughput screening is often constrained by a distinct mismatch between laboratory culturing conditions and real-world applications. Along similar lines, industrial approaches towards bioremediation often suffer from a lack of suitable test beds for screening different strategies, since the on-field deployment of this technology deals with granular, porous media such as sand and silt, which cannot be effectively replicated on laboratory workbenches. Considering these unmet challenges, in this work we target the following objectives:

1. Develop methods to design biomimetic 3D matrices that support the culture of a broad range of microbial strains
2. Modify these in vitro platforms to generate optically transparent 3D growth media,
3. Achieve tunable material properties which can be used to model the mechanical regimes encountered in biological samples such as mucus and soil
4. Understand how diverse microbial species directly isolated from viscoelastic biological habitats such as mucus grow in these systems
5. Characterize how altered biomimetic mechanical regimes regulate the growth dynamics of these bacterial strains
6. Interrogate if growth under physical confinement lead to selective advantages for certain bacterial species based on their morphological/genetic attributes, to understand whether the mechanical microenvironment can reshape community compositions at the population level
7. Derive a generalizable physical principle for explaining how growth under 3D physical confinement enforces constraints which selectively favor certain bacterial species over others

### 3. Methods

#### 3.1 Preparation and Characterization of 3D growth media

We prepare the 3D matrices by dispersing dry hydrogel granules of Carbopol C-980 (Lubrizol) at either a 0.50% or 0.85% (w/v%) concentration in 2% (w/v %) liquid LB (Sigma, LB Lennox) media. While preparing minimal media matrices, we replace LB media with M9 media (BD Difco, M9 Minimal Salts) supplemented with 0.2% glucose and 0.2% milk protein hydrolysate as a source of amino acids. The hydrogel suspension is vigorously stirred for at least 2 hours to ensure complete hydration of the dry granules. Since the Carbopol C-980 is a negatively charged hydrogel, we neutralize the pH of this suspension to 7.4 using 10N NaOH. At pH 7.4 the hydrogel granules or microgels swell maximally to an extent when individual granules jam against each other forming a transparent and disordered solid matrix. We determine the viscoelastic properties of jammed microgels using oscillatory shear rheology on a shear-controlled Anton Parr (MCR302e) rheometer with a roughened cone-plate measuring tool. We adjust the solid fraction of 3D growth media to achieve an elastic storage modulus range between 10 Pa to 110 Pa, that spans the measured range of biological mucosal samples. To measure the yield stresses and viscosity of the hydrogels, we apply unidirectional shear at varying rates while recording the shear stress response. As shown in Fig. 1, our microgels behave as yield stress materials, which are reversibly fluidizable upon application of the threshold shear rate but retain a soft solid-like nature below this regime. Porosity of the microgels are determined using 200 nm fluorescent tracer particles. We track the thermal diffusion of these beads through the inter-particle pore spaces. Since the internal mesh sizes of the hydrogel granules are smaller than 100 nm, the beads are occluded from these regions. Hence, the beads only explore volumes that are also accessible to bacteria (which are up to 10-fold larger in dimension than the bead size). We disperse a dilute solution of the tracer particles in both low and high confinement matrices. Subsequently, we acquire images within a time interval of 17 ms using the 40X objective of an inverted laser-scanning confocal microscope (Nikon A1R HD25) to track their thermal diffusion-guided trajectory. Individual beads are tracked with sub-pixel precision using a custom-written MATLAB script based on the Crocker-Grier algorithm<sup>62</sup>, and the mean-square displacement (MSD) is quantified as a function of lag time. Over short time scales, the particles freely explore the pore spaces. However, over longer time scales, their motion becomes constricted by the porous medium and its dead-end channels. This implies that the particle MSDs will increase linearly with time for unimpeded motions, while over longer time scales the pore boundaries will make the MSDs plateau. The characteristic smallest pore space dimensions explored by the particles is then given by the square root of these plateau values added to the particle diameter. We calculate the 1-CDF (complementary cumulative distribution function) of the measured pore spaces, which represents the overall pore size distribution within our 3D microgel growth media. Herein, the value of the 1-CDF at any given pore size represents the fraction of the pores which are larger than the given pore size. For instance, a 1-CDF value of 0.5 represents the 50th percentile of pore sizes. Similarly, a 1-CDF value of 0.05 denotes that 5% of the pores are larger than the corresponding pore dimension. (**Fig. 1c and 3c**). We also show that under the culturing conditions followed in this work, our microgel samples do not undergo any significant alterations to the rheological properties or bulk volumes. For this, we take the low confinement matrix, and maintain it at 30°C for up to 24 hours under humid conditions (**Fig. 3h**). This is similar to the assay set up for all our biological experiments. Further, we recover and pool together the microgel samples from these plates and carry out rheological

measurement as well as direct weighing to establish that both the rheological properties and the overall sample volume remains conserved (**Fig. 3h, 3i, and 3j**).

### **3.2 Isolation, *in vitro* culture, and characterization of bacterial strains**

We isolate seven different microbial species from red flour beetles (*Tribolium castaneum*) and identify these by Sanger sequencing of the 16S rRNA gene using the universal 16S primers 27F (5'-AGAGTTTGATCCTGGCTCAG-3'), and 1492R (5'-GGTTACCTTGTTACGACTT-3') (**Fig. 1b**). Following the alignment of both forward and reverse sequences, a homology search using NCBI BLAST is carried out to identify the closest bacterial species for each such amplicon. Primary isolates from these are cultured in 2% LB broth and cryopreserved as glycerol stocks (20% v/v). For each experiment, a shaken culture of 1% stock dilution in LB broth is grown at 30°C for ~20 hours to achieve a stationary phase culture. From this, a 1% inoculum is added to fresh 3D growth media and homogeneously dispersed by gentle pipette mixing. To promote better growth in the case of *E. faecalis* and *E. faecium*, overnight cultures are directly set using 3D hydrogel media. We also employ two strains of *E. coli* – one, the wild-type motile strain, and the second carrying a deletion in the flagellar gene *flhDC*, that renders it non-motile. For antibiotic treatment of *E. coli* with A22, we maintain a sub-MIC concentration of 1 µg/ml in LB and 5 µg/ml in 3D media. To characterize the bacterial morphology, we dilute samples using either LB or 0.5% 3D growth media and spread these on a flat agar pad (1% (w/v) agar in water), placed inverted onto a glass bottom dish. Images are acquired using a point-scanning laser confocal microscope. To measure the cellular morphology, we segment micrographs in ImageJ and use in-built functions to quantify the cell body area, length, and aspect ratio. We ascertain the suitability of LB broth as a nutrient medium for all bacterial strains by assaying their growth in shaken liquid cultures (**Fig. 2**). We separately assess the growth performance of these strains under non-shaken culturing conditions in liquid LB, results from which show that static culturing conditions in liquid media lead to less efficient growth for most microbial strains used in our study (**Fig. 6b**). We also quantify the viability of cells grown in the high confinement matrix. In all samples, we use propidium iodide (fluorescence in red) as a marker for dead cells, since this compound stains cells with compromised membrane integrity. We also use Calcein-AM Green as a marker for viable cells in the case of *E. faecalis* which shows good uptake of this compound. For the *E. coli* strains, we use the constitutively-expressed green fluorescent protein signal as a marker for viable cells. For viability testing, we culture different bacterial strains in the high confinement matrix for 24 hours, following which we dilute the samples in liquid LB, vigorously mix using vortexing to break apart colonies into single cells under mechanical shear, and incubate with the appropriate staining solutions, before spreading them on flat agar pads for image acquisition. To test for genomic DNA damage-triggered responses, we use *E. coli* strains carrying a constitutively-expressing GFP-tagged histone protein (HU-GFP) that marks the DNA, along with an mCherry-tagged DNA damage response-triggered protein (SulA-mCherry). These are cultured for 24 hours in microgels of different stiffnesses and imaged using a confocal microscope. As an additional control, we induce DNA damage in an exponential-phase culture of bacterial cells cultured in liquid LB by treating with 5 µg/ml of the DNA damage-inducing drug MMC, which exhibits strong SulA-mCherry expression.

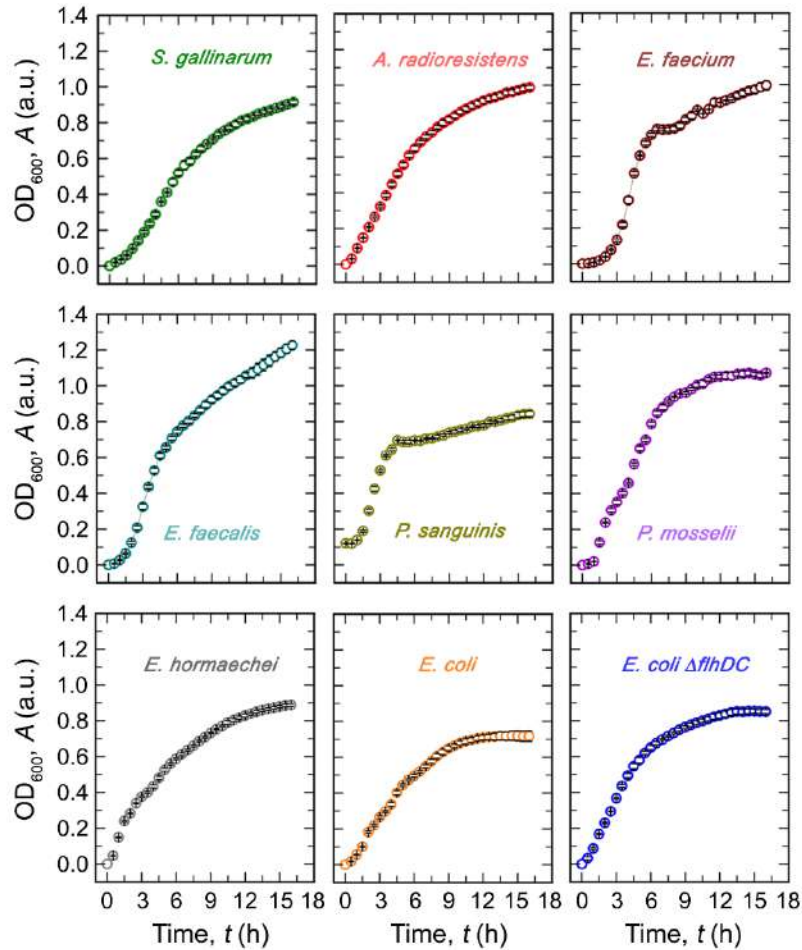


**Figure 2:** Absorbance-based growth curves for all bacterial strains in LB broth under continuously shaken culturing conditions (from 3 technical replicates).

### 3.3 Growth assays

We assay microbial growth in 3D growth media using absorbance-based optical density measurements at 600 nm. Samples prepared as described above are dispensed as 200  $\mu$ l replicates into 96-well plates, and readings are acquired at 10-minute intervals for 16 hours using a multi-mode plate reader (Varioskan Lux) with temperature control (set to 30°C). All data are normalized by subtracting the initial timepoint value (except for antibiotic-treated samples, where we normalize using the lowest absorbance value to account for initial cell death). This gives a measure of the net increase in biomass over time. For 3D co-culture assays, all parameters are maintained identical to the above, except the initial inoculum, wherein both competing strains are added in similar proportions by normalizing the optical density of overnight-grown cultures. To maintain identical culturing conditions as followed for the individual growth assays, we dispense these samples in a 96-well plate and grow them for 16 hours at 30°C. Following this, we pool together all the technical replicates for each gel type and homogeneously mix the sample. From this, a 20  $\mu$ l aliquot is used for direct bacterial counting, with the rest being processed for genomic DNA extraction (described below). For growth experiments where we vary the increase in osmotic pressure, we use varying amounts of the inert polymer PEG1000 doped in liquid LB. Here, we maintain the elevation in osmotic pressures to levels similar to the high confinement matrix (~110 Pa), as well as 10-fold and



100-fold higher. The osmotic pressures of these solutions are approximated using the equation  $\pi = icRT$ , where  $\pi$  represents the osmotic pressure,  $i$  denotes the van't Hoff index,  $c$  is the molar concentration of solute,  $R$  is the ideal gas constant, and  $T$  is the temperature.

### 3.4. Direct microscopic counting of single cells

Briefly, we set up growth curve assays for the non-motile *E. coli*  $\Delta flhDC$ , as described above, in multiple triplicate sets, for both low confinement and high confinement matrices. At specific time points separated by three-hour intervals, we obtain an optical density measurement for each set. Each individual replicate belonging to this set is harvested, mechanically sheared to break up colony-like clumps into single cells and diluted using LB (Fig. 3d). We scale the dilution factor for each timepoint following the first one to achieve approximately the same final density of bacterial cells. These samples are then mixed with microgel (to prevent cells from settling during the counting procedure) in a 1:1 ratio, following which 200  $\mu$ l of this sample is dispensed into a glass-bottomed 35 mm dish and fixed 3D volumes from each are imaged using a confocal microscope. The total number of bacteria is tallied using automated thresholding and segmentation functions available in ImageJ, as well as the 3D Cell Counter plugin. Using this, we calculate the number of bacteria per mL from the original sample and plot this against the measured absorbance value. We observe a roughly linear relation between the microscopically counted number of cells and the optical density of the sample, confirming that absorbance values provide an accurate estimate of the total bacterial biomass in 3D growth media. We also directly benchmark the volumetric counting method against the conventional colony forming units (CFU)-based quantification method. Herein, we prepare samples of bacteria inoculated in the microgel growth media. These are diluted in liquid LB and imaged using confocal microscopy to obtain the volumetric cell density as described above. Following this, the same samples are serially diluted using liquid LB and plated on LB agar. Colonies resulting from these are counted the next day and tallied against the statistics obtained from direct volumetric counting. We find a good agreement between both these metrics, which together with the optical density vs. volumetric counting approach, establish that direct counting using microscopy is a quantitatively rigorous method which compares well against both optical density and CFU-based quantification methods.

To verify this for the relative biomass ratio metric, we set up growth curve assays for both *A. radioresistens* and the non-motile *E. coli*  $\Delta flhDC$ , as described above, in both low and high confinement matrices. Immediately after the growth curve assay concludes, we pool together all replicate samples of each bacterial strain and each specific confinement type in separate microcentrifuge tubes. This is well-mixed to ensure homogeneous dispersion of the bacteria. 20  $\mu$ l of this is added to 1 ml of 0.50% microgel (to prevent cells from settling during the counting procedure) and mixed thoroughly to break up the colonies into single cells. 200  $\mu$ l of this sample is dispensed into a glass-bottomed 35 mm dish and imaged using a confocal microscope. From the images, individual bacteria are microscopically identified and tallied. We then compare the ratio of endpoint absorbances from 0.85% microgel to 0.50% microgel for both bacterial strains with the ratio of numbers obtained by direct counting for identical samples.

For the co-culture experiments from section 4.3, we prepare an inoculum with equal parts of both high aspect ratio cells (motile *E. hormaechei* or non-motile *E. coli*) and low aspect ratio cells (either *A. radioresistens* or *E. faecalis*), that we homogeneously disperse in both low and high confinement 3D growth matrices. Following sixteen hours of growth, we

mechanically disrupt the colonies in each matrix into homogeneously dispersed single cell suspensions. Subsequently, we spread these on flat agar pads (in the case of the *E. coli* vs *A. radioresistens* combination, we also include one replicate with volumetric 3D cell counting) and tally the number density of each type of bacteria using microscopy to obtain the relative number of cells belonging to each strain type per sample.

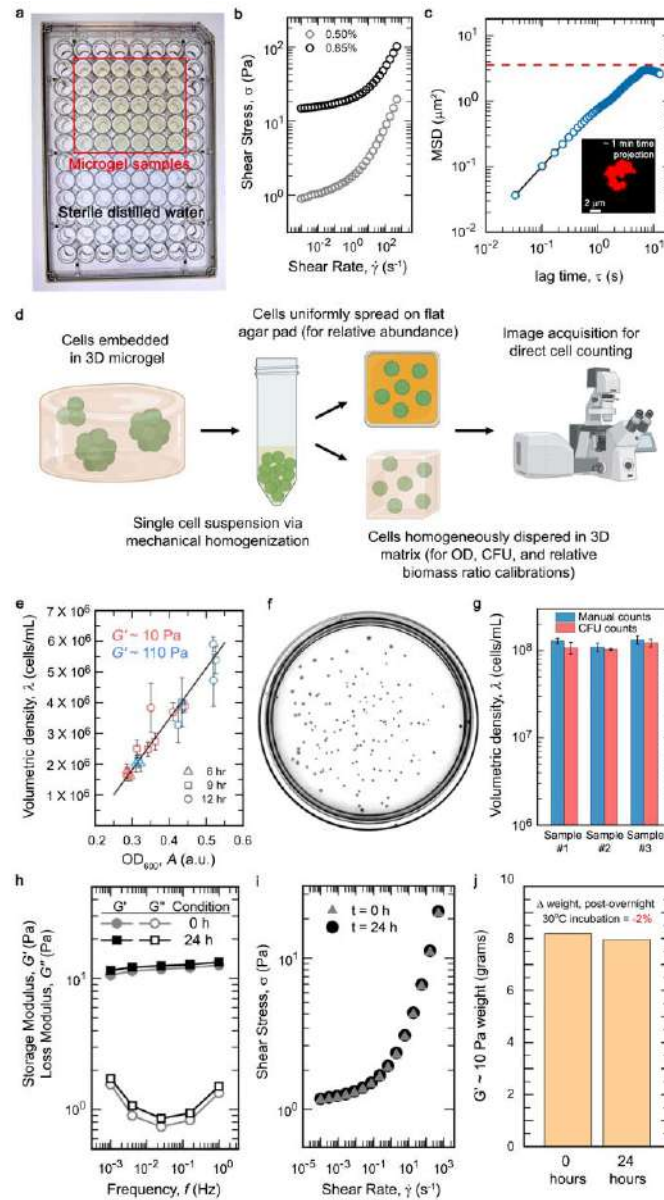


**Figure 3:** (a) Representation of the microgel-based culturing setup, wherein, bacteria-laden microgel samples are maintained in 96 well plates under humid conditions (by filling up surrounding wells with sterile distilled water) in 30°C to minimize evaporative losses. (b) Rheological measurements reveal that the 3D growth media behaves as a yield stress material – i.e., it undergoes reversible fluidization at high shear rates while behaving as a soft solid at low shear rates. (c) Representative particle tracking of a 200nm fluorescent tracer particle moving via thermal diffusion within the inter-particle pore spaces of the 3D microgel matrix. The plateau value represents the cage size of the pore that constrains the overall particle displacement. (d) Schematic representation of sample processing for direct cell counting. (e) A comparison between absorbance measurements and volumetric density of cells shows a broadly linear relation for both the low confinement and high confinement matrices, indicating

that the optical density-based absorbance measurements can be used as a reliable indicator of total bacterial biomass for the 3D growth media. Volumetric density is measured by directly counting the total number of cells present in a 3D volumetric image from confocal microscopy. (f and g) We directly benchmark the microscopic 3D volumetric counting method against conventional colony forming units (CFU)-based estimation of cell numbers and show good agreement between both. (h, i, and j) Culturing conditions do not cause appreciable changes to the rheological properties or bulk volume of the 3D microgel matrix, even for the low confinement system.

### 3.5. Colony morphology experiments

For live-cell imaging of bacterial colonies, we use 35 mm plastic dishes with a central circular cavity (15 mm in diameter) sealed off with a glass coverslip for optimal quality imaging. Samples for assessing the colony morphology are prepared exactly as described above for the growth curve experiments. While the *E. coli* strain used in this study shows constitutive expression of the green fluorescent protein, we use the cell viability dye Calcein-AM Green to stain *E. faecalis* cells (for live imaging, the dye is directly added to the microgel growth media). 200  $\mu$ l of well-mixed samples are dispensed into the glass-bottomed cavity of these dishes. Using a sterile coverslip, we scrape the top of this sample to ensure a smooth, flat layer. To prevent evaporative losses, we gently layer the top of the sample with 1.5 ml of mineral oil (Sigma). This oil is permeable to gases; hence the microgel-suspended bacteria are not cut off from oxygen supply. Plates prepared in this manner are placed in an incubator maintained at 30°C for 16 hours. Following this, we acquire z-stack images of the bacterial colonies using confocal microscopy. Colony morphology is analysed by segmenting 2D projections of the individual bacterial colonies, followed by calculation of the colony area and perimeter using in-built functions in Fiji-ImageJ. Using this, we calculate a parameter termed the shape factor, defined herein as the ratio between the perimeter and the square root of the area (for a circle, the shape factor equals 3.54). This quantity gives an estimate of how much colony shapes differ across various species and treatment conditions.

### 3.6. DNA Extraction and 16S rRNA amplicon sequencing

For genetic analysis of 3D media-grown and liquid ( $t_0$ , initial inoculum) co-culture samples, we carry out genomic DNA extraction. 300  $\mu$ l of each sample is incubated at 65°C for 2 hrs with 200  $\mu$ l of Promega nuclei lysis buffer, followed by the addition of 200  $\mu$ l Promega protein precipitation solution and 100  $\mu$ l of chloroform to promote phase separation. The DNA-containing fraction is separated out by centrifugation, to which 300  $\mu$ l isopropyl alcohol is added to precipitate the nucleic acids fraction. The resultant pellet is washed twice with 80% ethanol, following which we elute the genomic DNA in 40  $\mu$ L nuclease-free water. To determine the change in the relative proportion of the two co-cultured strains, we amplify the V3-V4 hypervariable region of the bacterial 16S rRNA gene using the modified Illumina 10N primer<sup>63</sup> and sequence amplicons on the Illumina Miseq platform (300x2 paired-end, obtaining ~75000-140000 reads per sample). We analyze sequence data using the DADA2 pipeline<sup>64</sup> in R, which gives us the relative abundance of each strain in each sample.

We also note that the trends observed using 16S rRNA amplicon sequencing-based methods are largely qualitative in nature. This is primarily due to experimental limitations with designing efficient cell lysis protocols for both competing strains, as well as difficulties with optimal DNA extraction from cells embedded in 3D microgel matrices (wherein, cross-reactivity and charge interactions of the extraction reagents with the scaffold material cannot

be entirely discounted). In this regard, the flexibility afforded by the matrix in terms of cell extraction and visualisation allow for parallel strategies such as direct counting of individual cell types, enabling a precise estimation of relative bacterial loads even from co-culture setups. However, direct visualisation and counting also comes with certain limitations. For instance, this strategy is only amenable for bacteria whose colonies can be sufficiently disrupted using mechanical shear without lysing the cells. Second, unless the competing strains are unambiguously distinguishable based on morphology (rod vs sphere) or visual contrast (e.g., fluorescently tagging/dye-based labelling or differential colorimetric staining), counting is not a reliable method. This limits its applicability for a select few combinations of bacterial strains. We believe that further work towards optimizing both 16S rRNA amplicon sequencing and visualisation-based approaches as well as developing hybrid workflows on a case-by-case basis will significantly improve the applicability of our 3D microgel matrix towards enabling a rigorous quantitative estimation of species-specific bacterial loads from mixed microbial communities cultured in vitro in 3D.

### **3.7. Simulating bacterial growth**

We simulate 3D colony growth using a previously published agent-based platform (CellModeller<sup>35</sup>) which models bacterial cells as spherocylinders. We modify the original code by altering the aspect ratio of these objects by explicitly defining the radius and overall volume, which together adjust the cell's length. Using this, we simulate 3D growth of either high-aspect ratio "rods", or low-aspect ratio "spheres". We trigger the cells to divide once they achieve a target volume greater than twice the defined volume for a single cell, with both resultant daughter cells starting off with the initial volume defined for a single cell. Further, we constrain the progeny cells produced by rods to maintain orientation along the parental axis, whereas the progeny cells produced by spherical cells are allowed to reorient in random directions. We also simulate different degrees of physical confinement by varying the environmental drag ( $\Gamma$ ) on the growing bacterial cells.

## 4. Results

### 4.1 Mimicking physical properties of the mucosal microenvironment

To understand how the physical properties of their microenvironment regulate bacterial growth, we avoid the use of laboratory strains to minimize potential experimental artefacts arising from laboratory adaptation, such as mutations accumulated during long-term culture in homogeneous liquid cultures or 2D surfaces. Hence, we isolate several bacterial strains from the gut of the red flour beetle (*Tribolium castaneum*) and identify them using 16S rRNA sequencing. These bacteria naturally reside in a viscoelastic microenvironment, which ensures minimal interference from culturing practices. Together, these strains include a diverse representation of different envelope properties, metabolic modes, motility patterns, and morphologies (**Fig. 1b**). To create a structural mimic of their natural habitat, we design a jammed microgel-based 3D growth medium that mimics the physical and structural properties of mucus (**Fig. 1c**). Previous structural analysis of mucus indicates different regimes of porosities, spanning from nanometer-scale to micron-scale pores<sup>25</sup>. Further, rheological measurements on mucosal samples from various sources also reveal a broad range of shear moduli (ranging from ~ 1 Pa to ~ 100 Pa) and viscosities (ranging from ~ 10 mPa.s to ~ 5 x 10<sup>5</sup> mPa.s)<sup>26</sup>. By packing micron-scale granules of hydrogels swollen in liquid LB (Luria-Bertani growth medium) beyond their jamming concentration, we manufacture a soft, semisolid 3D matrix with the key physical properties of mucus — especially the porosity ( $\psi$ ), shear moduli ( $G'$  and  $G''$ ), and viscosity ( $\eta$ ) (**Fig. 1d-1f, Fig. 3b and 3c**). The nanometer-scale internal mesh sizes of the polymer chains forming each hydrogel granule allow unimpeded uniform diffusion of nutrients and small molecules throughout the bulk medium<sup>27-29</sup>. The microparticles themselves pack together to generate micron-scale inter-particle pore spaces ( $\psi$ ), which provide a porous and internally disordered matrix for the bacteria. Within this, bacteria can move by exploring the tortuous pore spaces, as well as achieve 3D colony growth by pushing aside the microparticles to locally and reversibly deform the matrix. Importantly, our 3D microgel growth media retain soft solid-like bulk properties under low shear, while being reversibly fluidizable upon application of shear rates higher than the yield stress limit—which is orders of magnitude lower than the internal turgor pressure of typical bacterial membranes. This allows bacterial colonies to internally rearrange the 3D matrix during growth without altering its material properties, allowing us to reproducibly maintain stable mechanical regimes over long-term culture. Using these platforms, we ask how two different degrees of confinement—representing both extremes of the physical regimes commonly observed for naturally occurring mucus—alter bacterial growth.

### 4.2 Bacterial growth varies with confinement

The 3D growth medium comprises a low solid fraction, which lends it high optical transparency allowing us to directly visualize bacterial growth under physical confinement. Leveraging this physical property, we homogeneously disperse bacteria in both low confinement and high confinement matrices and employ standard optical density-based absorbance measurements for assaying the temporal change in bacterial biomass (**Fig. 4a**). Optical density measurement ( $A$ ) in these matrices is linearly proportional to the volumetric

1 density of bacterial cells ( $\lambda$ ) as obtained by direct counting from micrographs. Our volumetric  
2 counting method is quantitatively robust as it correlates well with the conventional colony forming  
3 units (CFU)-based assay for identical samples (**Fig. 3e, 3f, and 3g**). Interestingly, we observe  
4 a decrease in the overall biomass production for all bacterial strains with an increase in  
5 confinement (**Fig. 4b and Fig. 5**). Prior reports suggest that the growth of bacteria is altered  
6 under elevated hydrostatic pressure, well above the turgor pressure of bacteria, which may  
7 lead to deformation of the cell shape and induced stress response<sup>30,31</sup>. However, since the  
8 elastic modulus of the microgel growth media is approximately three orders of magnitude lower  
9 than the internal turgor pressure of bacterial cells<sup>32</sup>, the observed reduction in overall biomass  
10 production is likely not due to compressive deformation of the cell body. To rule out aberrant  
11 effects of elevated osmotic stress on bacterial growth, we culture bacteria in liquid LB broth  
12 doped with varying amounts of the bioinert polymer PEG-1000 that induces an increase in  
13 osmotic pressure up to 100-fold higher than that exerted by our highest degree of 3D  
14 confinement. We find minimal effects on bacterial growth (**Fig. 6a**). We further verify that our  
15 3D matrices do not significantly affect cellular morphology. We negate the possibility of body  
16 deformation under 3D confinement by morphometrically analysing the cells; in both low and  
17 high confinement matrices, cell morphology remains identical, indicating that growth decrease  
18 under higher confinement is not due to decrease in cell sizes. (**Extended data Fig. 7a, 7b,**  
19 **and 7c**). Further, we show that the observed growth patterns cannot be attributed to cell death  
20 by quantifying the cell viability in the microgel growth medium. These results show that growth  
21 under high confinement does not detrimentally affect the proportion of viable cells in the  
22 population (**Fig. 7d and 7e**). To further ensure that an increase in confinement does not cause  
23 detrimental effects on cellular physiology, we also culture a genetically modified *Escherichia*  
24 *coli* strain— engineered to visually report both the genome's physical organisation using HU  
25 (a DNA-binding protein) tagged to GFP, as well as induction of SulA-driven DNA damage  
26 responses — in 3D microgel growth media of both low and high degrees of confinement (**Fig.**

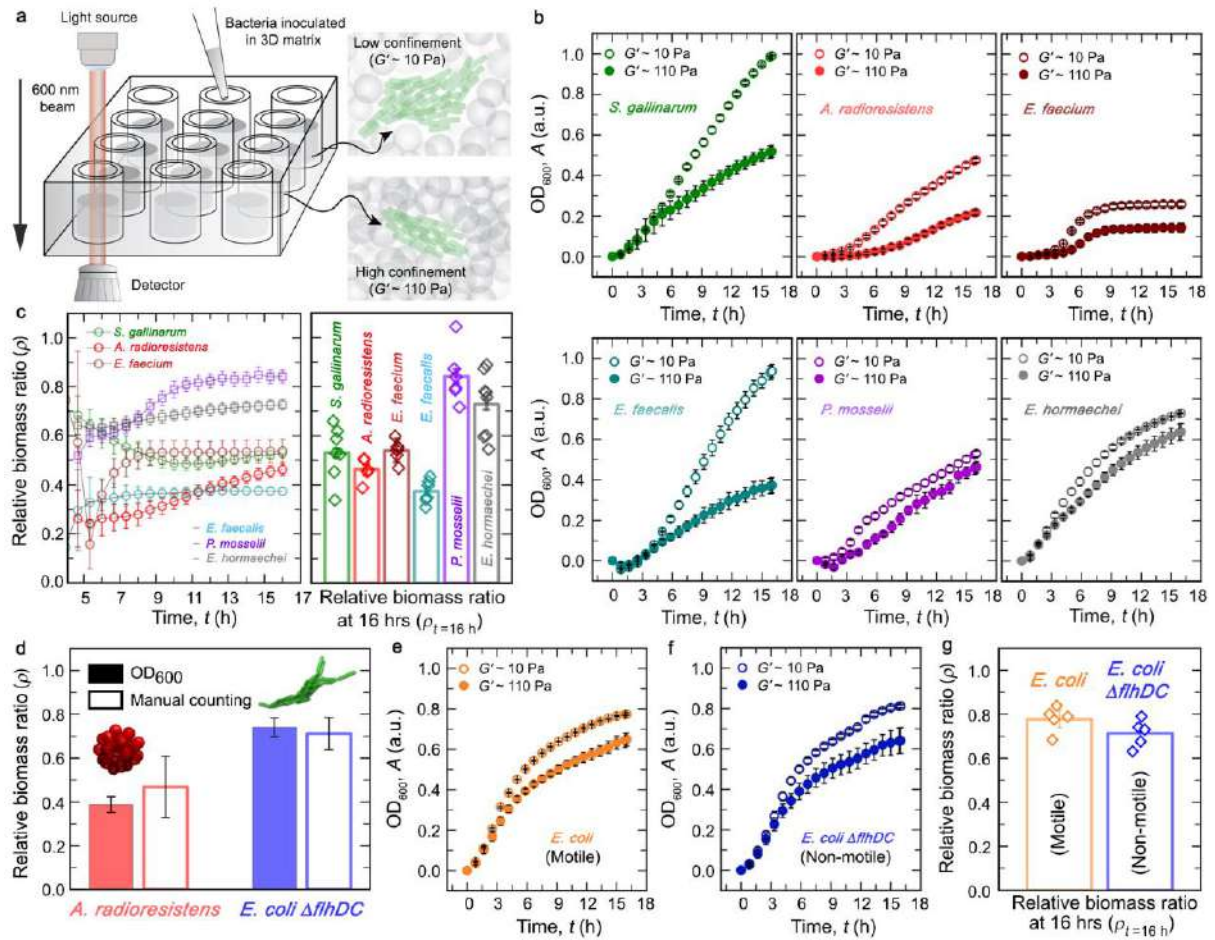


**Figure 4: Change in confinement alters bacterial population growth.** (a) We use absorbance-based optical density measurements as an indicator of increase in biomass over time to quantify bacterial growth in the 3D microgel media. (b) Representative absorbance-based growth curves over 16 hours indicating confinement-dependent growth dynamics for all bacterial strains (mean  $\pm$  s.d.,  $n = 3$  technical replicates);  $G' \sim 10$  Pa represents low confinement matrix and  $G' \sim 110$  Pa represents high confinement matrix. (c) Relative biomass ratio values for all bacterial strains across all time points, showing that higher confinement demarcates the different microbial species into two distinct subgroups, indicated by bar graphs representing the plateau value of the relative biomass ratio at 16 hours (mean  $\pm$  propagated error,  $n \geq 4$  biological replicates). (d) Absorbance measurements from 3D growth media mirror the actual microbial load, determined by measuring volumetric bacterial density via direct counting of cells using 3D confocal microscopy (also see Extended data fig 2b). Both of these measurements yield comparable relative biomass ratio after 16 hours of growth (mean  $\pm$  s.d.,  $n \geq 3$  technical replicates/micrographs). (e-g) Motility does not confer significantly greater fitness benefits under confinement, as tested using a motile and non-motile strain of *E. coli* (the latter carries a deletion in the flagellar protein-encoding gene *flhDC*), which show no significant differences between the growth curves (mean  $\pm$  s.d.,  $n = 3$  technical replicates) or the relative biomass ratio (mean  $\pm$  propagated error,  $n = 5$  biological replicates).

7f). We observe that increase in physical confinement neither alters the HU-GFP localization pattern (i.e., no observable change in the genome's spatial arrangement<sup>33</sup>) nor induces Sula expression (indicating DNA damage responses are not triggered<sup>34</sup>). Hence, the decrease in biomass production under higher confinement is likely not due to altered growth patterns such as those triggered by DNA damage-induced stress responses.

To quantify the impact of confinement on growth, we normalize the biomass achieved at each timepoint in the high confinement matrix ( $A_{\text{high}|16\text{h}}$ ) to that in the low confinement matrix ( $A_{\text{low}|16\text{h}}$ ) for each strain, which gives the relative biomass ratio ( $\rho$ ). This parameter initially



varies with time, before achieving a plateau over twelve to sixteen hours for all strains, indicating the existence of a general, non-species-specific effect of confinement on bacterial growth (Fig. 4c). To focus on these effects at a stable time point, we quantify the endpoint biomass ratios at the sixteen-hour mark and observe that strains cluster into two well-separated groups—those which perform poorly under increased confinement, and those which remain relatively less perturbed (Fig. 4c). For additional rigor, we directly benchmark measurements of endpoint absorbance ratios against volumetric density of bacterial cells as obtained by microscopic counting from the same samples. Importantly, we perform these confirmatory tests for cells possessing two different shapes—approximately spherical and rod-like—thereby establishing the relative biomass ratio ( $\rho$ ) as a generalised quantitative measure of change in bacterial biomass in 3D matrices (Fig. 4d).

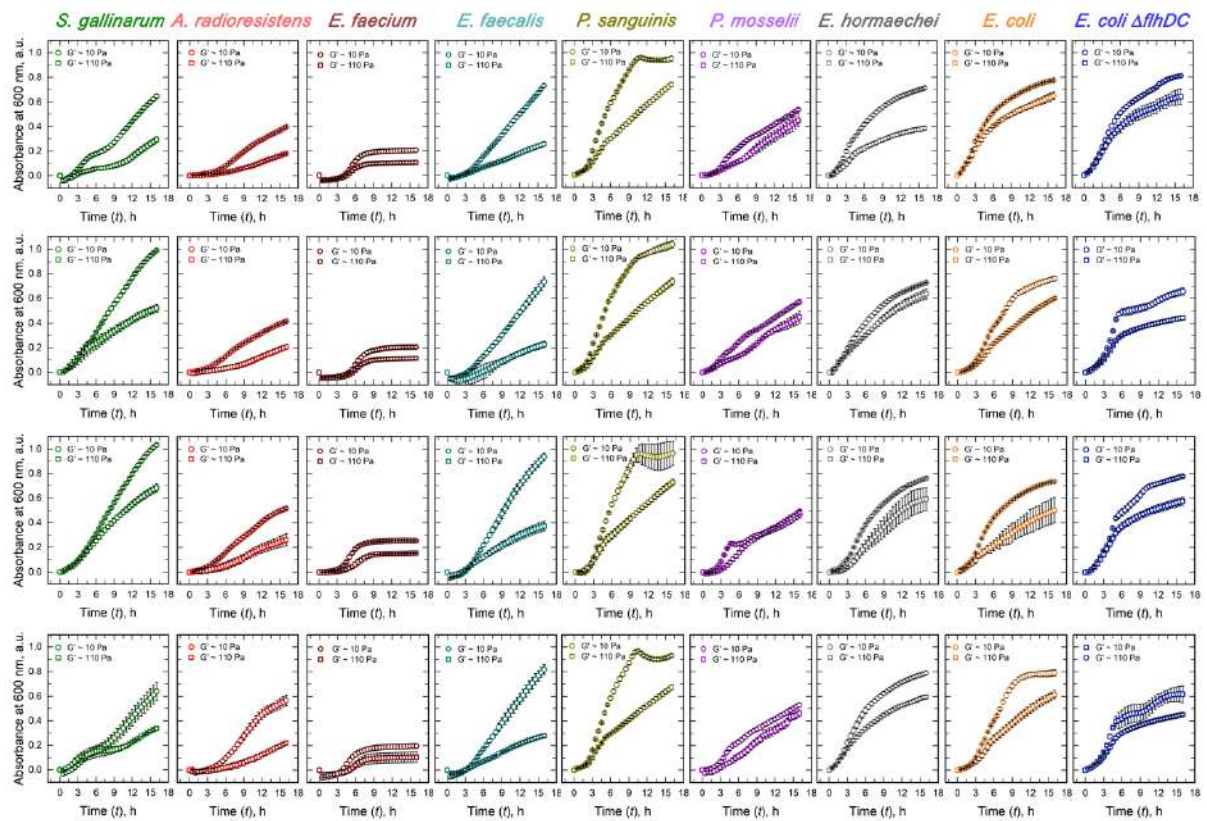


**Figure 5:** Representative biological replicates from growth curve assays in 3D microgel growth media for all bacterial strains used in this study.



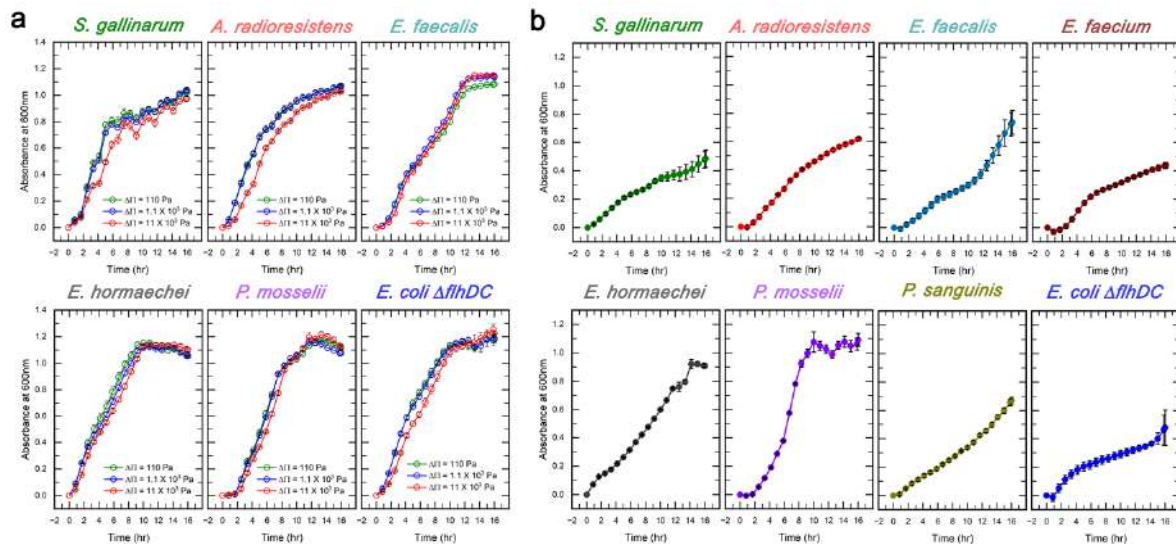


**Figure 6:** (a) Growth curves of three spherical and three rod-shaped bacterial strains in shaken liquid LB, with different degrees of osmotic pressure elevations achieved by adding the inert polymer PEG1000 to these cultures. No significantly detrimental effect of increased osmotic pressure on bacterial growth is observed. (b) Non-shaken liquid LB cultures of all bacterial strains used in this study. Static culturing conditions in a liquid media do not promote effective microbial growth.

A comparison of the various strain-specific morphological attributes listed in Fig. 1b reveals motility and cell body shape as distinguishing features of the two clusters observed in Fig. 2D. Since motility can conceivably allow better dispersion of bacteria in the 3D matrix<sup>24</sup> — thereby improving overall population-level growth through better nutrient accessibility and lesser local crowding—we first test the impact of motility on enhancing growth by employing both a motile (wild-type) and non-motile strain of *E. coli* (harbouring a deletion of a flagella-encoding gene). Surprisingly, both strains perform similarly under different degrees of confinement as captured by their relative biomass ratio ( $\rho$ ) (**Fig. 4e-4g, Extended data Fig. 7g and 7h**), invalidating motility as the dominant feature mediating the growth patterns observed under increased confinement. Consequently, we revisit the set of species-specific morphological attributes and note that while all poorly-performing strains comprise low aspect ratio (approximately spherical) cells, the better-performing strains have high aspect ratio cells (rod-like). These effects are not due to different biological species possessing intrinsically different growth rates. Although we observe that the absolute growth of certain coccoidal species is higher than some bacilli in the low confinement matrices, the relative biomass ratio metric specifically captures the performance of a given strain across two different degrees of confinement and is hence agnostic to how any other species fares. Using this, we observe a specific trend favouring a particular class of bacteria over others only when analysed along the shape axis. This observation forces a significant realignment of our perspective on growth under confinement, implicating cellular morphology as the attribute critical to growth success under spatial constraints.

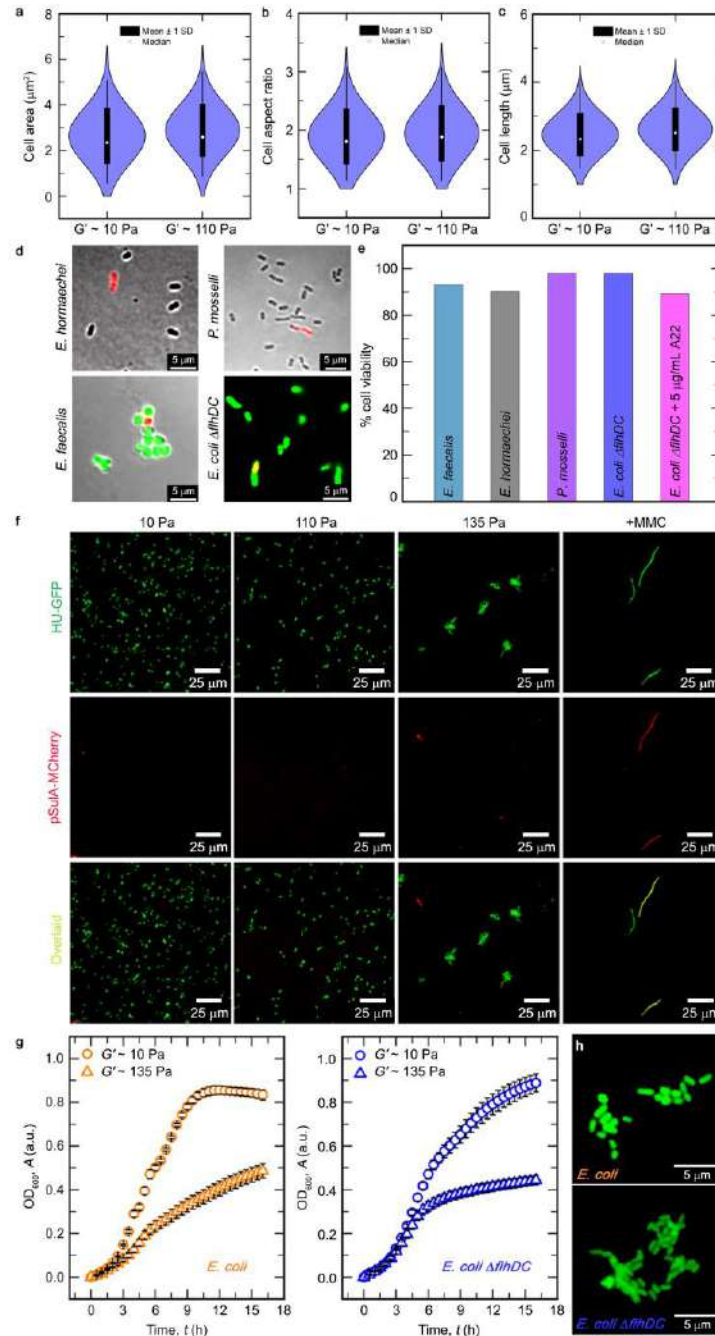


**Figure 7:** (a-c) The degree of physical confinement within jammed microgel growth media does not alter the cellular morphology of bacterial cells, as shown here for non-motile *E. coli* cells. (d and e) Growth under 3D confinement does not detrimentally affect the viability of bacterial cells. Staining using propidium iodide (red) as a marker of membrane-compromised cells (presumed dead), combined with calcein-AM (green) for *E. faecalis* and constitutive GFP expression for *E. coli* show that following 24 hours of growth in a high confinement matrix, population-level cell viability remains high ( $\sim \geq 90\%$ ) across several different microbial strains used in this study. (f) Growth under confinement does not affect the genomic integrity of bacteria, as evidenced by the lack of DNA damage response reporter (SulA, tagged to MCherry) expression. The HU-GFP indicates the genome organisation, since HU is a DNA binding protein. Hence, the signal in the green fluorescence channel indicates the genomic organisation of the *E. coli* grown under confinement. The SulA-Mcherry indicates triggering of

DNA damage responses, hence the signal in the red fluorescence channel marks out cells which show DNA damage response. Since we did not observe any noticeable levels of this signal from cells grown under physical confinement in our 3D microgel matrices, we went a step further and directly induced DNA damage to cells grown in liquid using the drug MMC, which has been included as a positive control. (g) Motility does not confer significantly greater growth benefits under confinement. Using highly confined microgel growth media, we observe that both motile and non-motile *E. coli* perform similarly. (h) Here we show that under high degrees ( $G' \sim 135$  Pa microgels) of 3D confinement, both motile and non-motile *E. coli* form elongated colonies. Typically, if a matrix allows for mobility, a motile strain is expected to disperse evenly and undertake single cell-driven growth. However, once we restrict the bacteria under sufficiently high degrees of 3D confinement, we observe that even motile bacteria are now forced to adopt a more localized, colony-driven form of growth, as their spatial dispersal is significantly hindered.

### 4.3 Single-cell morphology dictates colony shape

Unlike growth on homogeneous 2D interfaces or in well-mixed liquid media, growth under physical confinement imposes spatial constraints and consequent nutrient limitations on bacterial colonies. To determine how different single-cell morphologies affect colony architecture, we employ an agent-based simulation using the CellModeller platform<sup>35</sup>, maintaining all growth parameters constant and only altering the cellular aspect ratio. We simulate growth undertaken by low aspect ratio (approximately spherical) and high aspect ratio (rod-shaped) cells (**Fig. 8a**). While most high aspect ratio bacilli (rod-shaped) cells such as *E. coli* exhibit cell division patterns that produces progeny cells oriented along the parental cell's longitudinal axis, several low aspect ratio coccoid (spherical) species show planes of division that are either randomly or perpendicularly positioned to previous division planes, which allow a higher degree of freedom for the orientation of progeny cells following division<sup>36</sup>. We incorporate these patterns in our simulations by implementing that high aspect ratio bacteria divide and produce progeny oriented along the length of the parent cell, whereas low aspect ratio bacteria produce progeny oriented along a randomly chosen direction. Under these conditions, striking differences emerge, wherein the high aspect ratio bacteria generate elongated colonies, while the low aspect ratio bacteria give rise to rounded 3D colonies. We further characterise these using a parameter termed the shape factor ( $\phi$ ), defined as the ratio between the perimeter and square root of area for the projection of a given colony. A low value for the shape factor ( $\phi$ ) indicates that the colony has a relatively lower exposed surface area as opposed to the enclosed volume. We find that the low aspect ratio bacteria predominantly organise into colonies with a low shape factor, and the high aspect ratio bacteria form elongated, high shape factor colonies (**Fig. 8e, Fig. 9d, and 9e**). Hence, single cell morphology appears to strongly

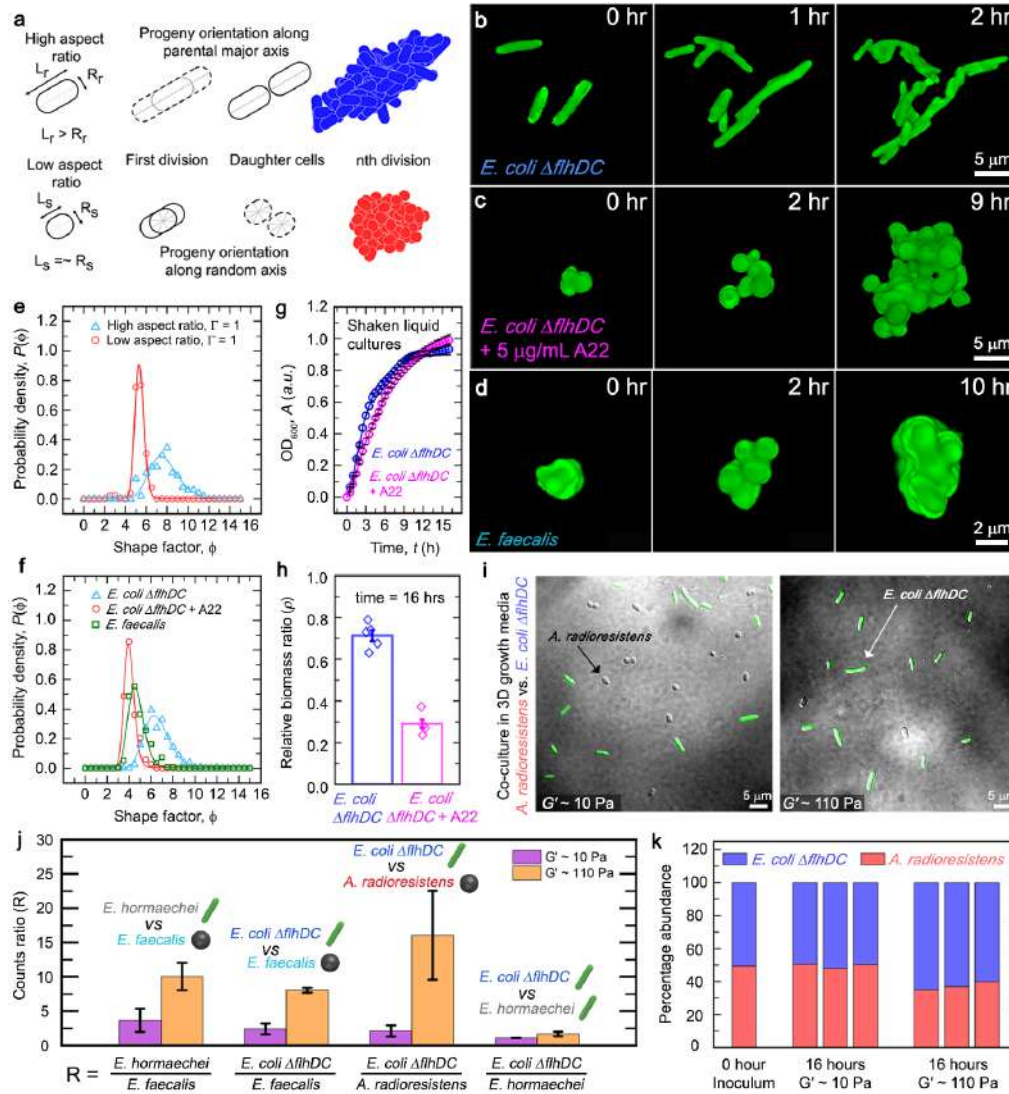


**Figure 8: Bacterial morphology determines colony architecture and competitive outcomes.** (a) We perform agent-based simulation of 3D colony growth for both high and low aspect ratio cells. In these simulations, progeny of high aspect ratio cells exhibits a directional bias along the parental axis, whereas those of low aspect ratio cells are more flexible to grow along any random axis. (b) Rod-shaped high aspect ratio *E. coli* cells give rise to elongated colonies under confinement as they proliferate by pushing their progeny outwards. (c) Treatment with 5  $\mu g/mL$  of the MreB-perturbing compound A22 produces approximately spherical *E. coli* cells, which result in a rounded colony architecture. (d) Naturally spherical *E. faecalis* cells, stained here with Calcein-AM Green, show division and colony formation patterns similar to that predicted by the simulations for low aspect ratio cells as well as the drug-treated spherical *E. coli* cells. Micrographs in (b), (c), and (d) are generated by capturing the front view of a 3D volumetric projection. (e and f) Quantitative analysis of colony morphology using the shape factor (ratio between perimeter and square root of the area obtained from 2D projections of colonies) shows a significant difference between high and low aspect ratio cells, for both computational simulations ( $n \geq 200$ , from 10 simulations) and experiments ( $n \geq 200$ ). (g) Shaken liquid cultures in LB media for both rod-shaped *E. coli* and A22-treated spherical *E. coli* cells do not show any significant differences in their overall growth. (h) Relative biomass ratios for rod-shaped and spherical *E. coli* indicate that rod-shaped cells are less affected than spherical ones under increased confinement, i.e., have  $\rho$  values closer to 1 (mean  $\pm$  propagated error,  $n \geq 4$  biological replicates). (i and j) Direct visualization and endpoint counting of cells from 3D co-culture assays including both low aspect ratio (*A. radioresistens* or *E. faecalis*) and high aspect ratio cells (motile *E. hormaechei* or non-motile *E. coli*) show that the latter enjoy a growth advantage under increased confinement, at the expense of the former. However, competitive cultures between two rod-shaped strains do not show significant enrichment of either strain. (mean  $\pm$  s.d.,  $n \geq 2$  biological replicates). (k) Analysis of genomic DNA extracts from similar 3D co-culture setups confirm that high aspect ratio bacteria are more robust to increase in physical confinement compared to low aspect ratio cells ( $n = 3$  biological replicates).



dictate overall colony architecture.

We experimentally test this by live imaging the 3D colony growth of non-motile rod-shaped *E. coli* under high confinement matrices and observe patterns consistent with our computational model. Rod-shaped *E. coli* cells undertake volumetric growth along the parental axis, and push their progeny cells outward, leading to elongated colony architecture (**Fig. 8b and Fig. 9a**). Next, to test these patterns using a spherical bacterial species, we fluorescently label *E. faecalis* cells using Calcein-AM Green. Time lapse imaging shows that these coccoid cells also follow a colony growth mode similar to that predicted for low aspect ratio cells by the simulations, by organizing into well-rounded colonies (**Fig. 8d, Fig. 9c, and Fig. 12d**). Further, we directly alter the morphology of non-motile *E. coli* using sub-MIC dosages of the MreB-perturbing compound A22<sup>37</sup>. Sub-lethal concentrations (5  $\mu\text{g/ml}$ ) of the drug induce aberrant division, rendering the rod-shaped *E. coli* into spherical cells. Again, as predicted by our computational model, the A22-treated low aspect ratio cells assume a rounded colony morphology (**Fig. 8c and Fig. 9b**). By quantitatively analysing the shape factor ( $\phi$ ) of the max projected fluorescent micrographs of colonies formed by rod-shaped and spherical cells, we find both the experimental and computational data to be in good agreement, with the single cell morphology being strongly implicated as the key determinant of colony-level organisation under 3D growth conditions (**Fig. 8f**).

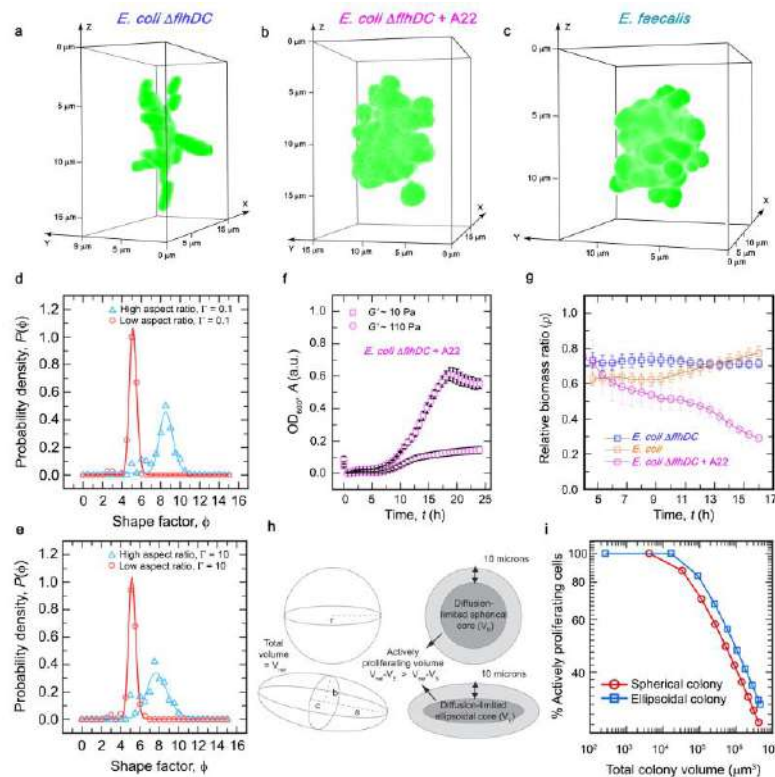


**Figure 9:** (a, b, and c) 3D reconstructions of colonies formed by rod-shaped *E. coli*, approximately spherical *E. coli*, and naturally spherical *E. faecalis* during growth in the high confinement matrix. (d and e) Quantitative analysis of colony morphologies using the shape factor metric, generated using simulations with different conditions of environmental drag ( $\Gamma$ ) on bacterial growth. In all cases, a clear distinction is visible between colonies formed by high vs. low aspect ratio bacteria, with the former organizing into colonies with a high shape factor value (more elongated), whereas, the latter organizes into more rounded colonies with a low

shape factor value. (f) Representative growth curves of *E. coli* treated with A22 under two different degrees of confinement, assayed for 24 hours of growth, considering the antibiotic-induced delay in proliferation. (g) Relative biomass ratio ( $\rho$ ) across 16 hours of growth under confinement for *E. coli*, non-motile *E. coli*, and non-motile *E. coli* treated with A22, showing how a shift in the bacterial shape towards approximately spherical morphology dramatically diminishes the relative growth success under increased confinement. (h) Schematic representations of numerical calculations considering either spherical colonies formed by low aspect ratio ( $=1$ ) cells or ellipsoidal colonies formed by high aspect ratio ( $=4$ ) cells. From previous work on *E. coli* confined in 3D porous media, we assume a maximum depth of  $\sim 10$   $\mu\text{m}$  up to which nutrient diffusion allows active proliferation of cells, beyond which the colony's core remains nutrient limited and hence metabolically inactive. (i) The proportion of actively proliferating cells in colonies of different sizes for either condition, showing that ellipsoidal colonies formed by high aspect ratio cells retain a significantly higher proportion of cells in the actively proliferating fraction, compared to spherical colonies formed by low aspect ratio cells, for colonies of comparable sizes.

#### 4.4 Confinement selectively favours rod-shaped cells

A comparison of the relative biomass ratio ( $\rho$ ) for rod-shaped and spherical *E. coli* reveals that alteration in shape severely compromises growth success under increased confinement, mirroring the trends exhibited by high and low aspect ratio gut-derived bacteria. Under similar concentrations of drug treatment ( $5 \mu\text{g/ml}$  A22), no significant growth differences are observed in liquid media. (**Fig. 8g and 8h, Fig. 9f and 9g**). In fact, the relative biomass ratio of the spherical *E. coli* is quite similar to that of the naturally low aspect ratio cells (approximately  $\rho \leq 0.5$ ). Together, these observations highlight how cellular morphology enforces differences in the colony architecture of rod-shaped and spherical cells during growth under confinement. We further find that these trends depend only on the cellular shape rather than other environmental variables. To test this hypothesis, we first alter the nutrient composition for the 3D matrices from rich LB broth to minimal media (M9) supplemented with glucose and amino acids (**Fig. 11a and 11b**). When cultured in the minimal media matrices, high aspect ratio *E. coli* and low aspect ratio *A. radioresistens* mirror the relative biomass ratio trends observed in LB-based matrices, indicating that the relative biomass ratio patterns are independent of nutrient composition (**Fig. 11c-11e**). The above results lead to the prediction that all else being equal, rod-shaped bacteria should have a growth advantage over spherical bacteria under higher confinement. We additionally verify this using numerical calculations of bacterial colony growth, wherein we consider two different colony architectures—ellipsoidal and spherical—formed by high aspect ratio rod-shaped bacteria and low aspect ratio spherical bacteria, respectively. The effective local concentration of a nutrient inside a 3D bacterial colony is a result of two processes: replenishment of small nutrient molecules via unimpeded diffusion and depletion of nutrients via consumption. The competition between consumption and diffusion sets a depth of  $10 \mu\text{m}$  from the surface of a 3D bacterial colony beyond which the nutrient is completely depleted<sup>20</sup>. Factoring in this previously established limit on effective nutrient availability inside a 3D bacterial colony—which sets a limit on the actively proliferating fraction of a given 3D bacterial colony—we estimate the proportion of actively growing bacterial cells in colonies of either geometry with different sizes (**Fig. 9h and 9i**). Ellipsoidal colonies comprising of rod-shaped cells retain a higher proportion of cells in the actively growing zone as opposed to spherical colonies of comparable sizes. Together, the above

results indicate that high aspect ratio bacteria produce elongated colonies, which allow better nutrient access in a 3D matrix, thereby enabling superior growth under increased confinement.

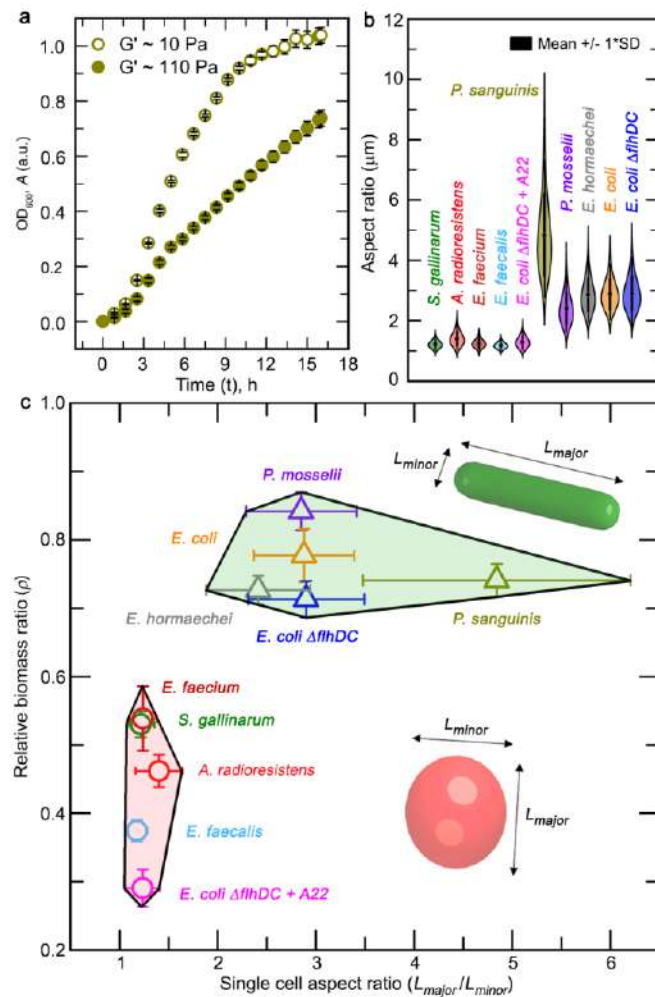


**Figure 10: Single cell morphology enables physical confinement to selectively favour elongated colony architecture** (a) Growth assays indicate that *P. sanguinis* performs at par with rod-shaped bacteria across two different degrees of confinement (mean  $\pm$  s.d.,  $n = 3$  technical replicates). (b) Measurements of the aspect ratios of bacterial cell bodies for all ten strains used in this study, measured from samples in the late exponential phase ( $n \geq 80$ ). (c) Microbial growth under confinement, as described using a phase space defined by the relative change in biomass production under increased confinement (the relative biomass ratio) vs. single cell morphology (mean  $\pm$  propagated error).

To test whether this effect provides a competitive advantage to high aspect ratio cells in a mixed population, we carry out co-culture assays that combine both high aspect ratio and low aspect ratio cells across two different degrees of confinement (**Fig. 8i-8k, Extended data Fig. 12a, 12b, and 12c**). For this, we prepare an inoculum with equal parts of both high aspect ratio cells (motile *E. hormaechei*, motile *P. mosselii*, or non-motile *E. coli*) and low aspect ratio cells (either *A. radioresistens* or *E. faecalis*), that we homogeneously disperse in both low and high confinement 3D growth matrices. Following sixteen hours of growth, we mechanically disrupt the colonies in each matrix into homogeneously dispersed single cell suspensions. Subsequently, we tally the number density of each type of bacteria using microscopy to obtain the relative strain ratios for each competing pair. As expected, the relative proportion of high aspect ratio cells in the population significantly increases with an increase in confinement, at the cost of a large decrease in the abundance of low aspect ratio cells (**Fig. 8i, 8j, and Fig. 12a**). Interestingly, an increase in confinement does not alter the relative abundance of two high aspect ratio species in direct competition (**Fig. 8j and Fig. 12b**). Parallely, we also perform bulk genomic DNA extraction and quantify

the relative abundance of each strain using 16s rRNA amplicon sequencing. Our bulk genomic analysis qualitatively mirrors the trends observed with microscopic tallying of the number density: despite identical nutrient media, rod-shaped bacteria gain a substantial advantage over spherical bacteria under high confinement (**Fig. 8k and Fig. 12c**). These results thus validate high aspect ratio morphology as a beneficial attribute under spatially confined growth. Of course, in many ecological settings, inter-species interactions are also heavily influenced by cross-feeding, cooperative and antagonistic behaviours, fluctuations in the environment, resistance to invasion, predation, and chemical cross-signalling<sup>1-6</sup>. Our platform presents the

capability to conserve the heterogeneous chemical and behavioural landscapes introduced by such variables, and study how physical confinement acts on top of these processes. This is because the porous nature of our matrix allows for unimpeded small molecule diffusion<sup>27–29</sup> regardless of the degree of confinement ensuring that modulation of the mechanical regime can occur independent of all other factors.

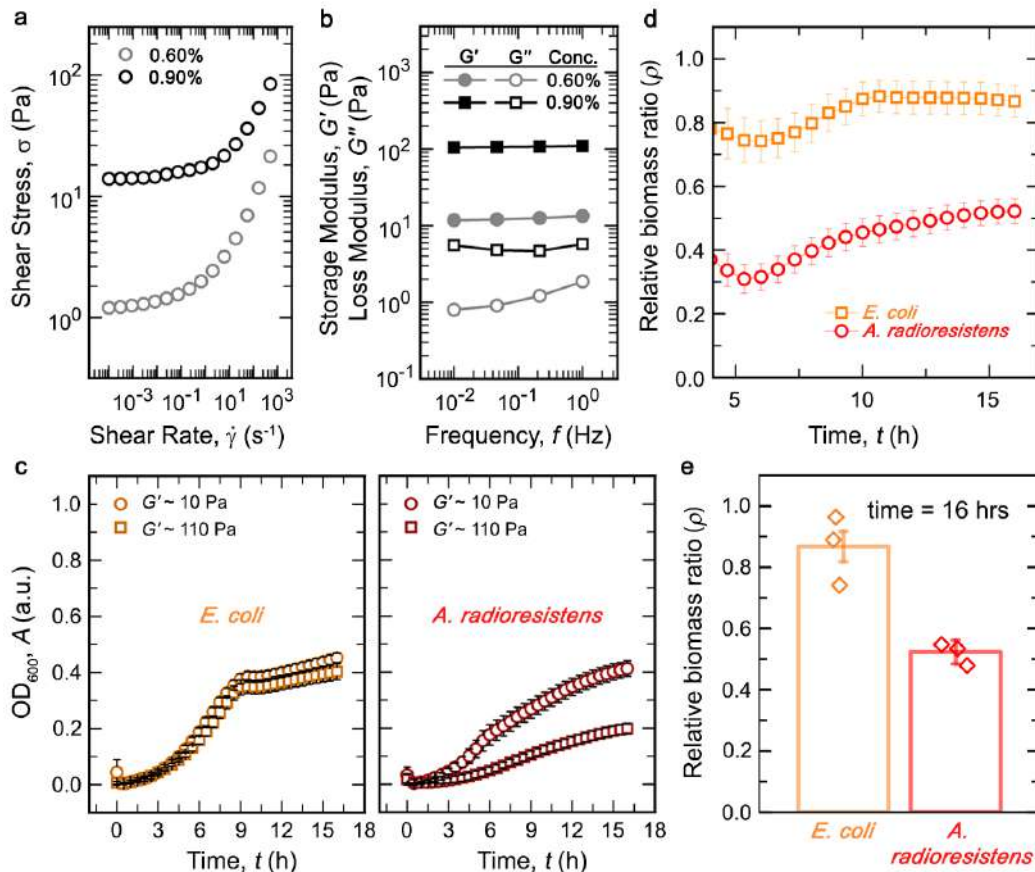


**Figure 11:** Characterizing bacterial growth dynamics in minimal media (M9)-based jammed microgel matrix. We replicate conditions of confinement similar to those imposed by the LB-based microgels using M9-based 3D growth matrix. (a and b) Rheological characterization of M9-based microgels reveals physical properties matching that of LB-based 3D growth media. (c) To test whether the trends exhibited by relative biomass ratios for low and high aspect bacteria are independent of nutrient composition, we assay the high aspect ratio *E. coli* and low aspect ratio *A. radioresistens* in minimal media (M9) supplemented with 0.2% glucose and 0.2% milk protein hydrolysate. (d and e) Relative biomass ratio trends over 16 hours of growth for the rod-shaped *E. coli* and spherical *A. radioresistens* across two different degrees of confinement using M9-based jammed microgel growth matrix. The results recapitulate what has been observed using LB-based 3D growth matrix, with the high aspect ratio *E. coli* exhibiting a superior relative biomass ratio under a higher degree of confinement.

In nature, cells exhibit morphological alterations under specific environmental conditions. For instance, uropathogenic *E. coli* transition between coccoid and rod-like morphologies during infection progression<sup>38</sup>. However, these transitions are also subject to chemical signalling and nutrient availability. These are best illustrated by examples such as those of *V. cholerae*, which shows a curved rod-to-sphere transition in response to both low temperatures or L-arabinose treatment, as well as *L. monocytogenes* that undergoes a similar



transition during biofilm formation on surfaces<sup>39–42</sup>. Such shape changes likely confer survival advantages under suboptimal conditions such as extreme environmental changes or nutrient starvation. However, it is also conceivable that a sphere-to-rod transition might prove particularly beneficial purely in terms of nutrient availability in porous 3D environments such as tissues and soil by promoting more efficient growth and proliferation. We test this hypothesis using *P. sanguinis*, a species wherein the spherical form can grow in an elongated fashion as a rod — similar to previous reports on *P. denitrificans*<sup>43,44</sup> (**Fig. 10a, Fig. 12e and 12f**). We assay the growth of *P. sanguinis* across two different degrees of confinement and find that it mimics the relative biomass ratio trend observed for high aspect ratio bacteria. This further validates that the elongated colony structure of high aspect ratio strains confers a relative advantage under increased degrees of confinement.

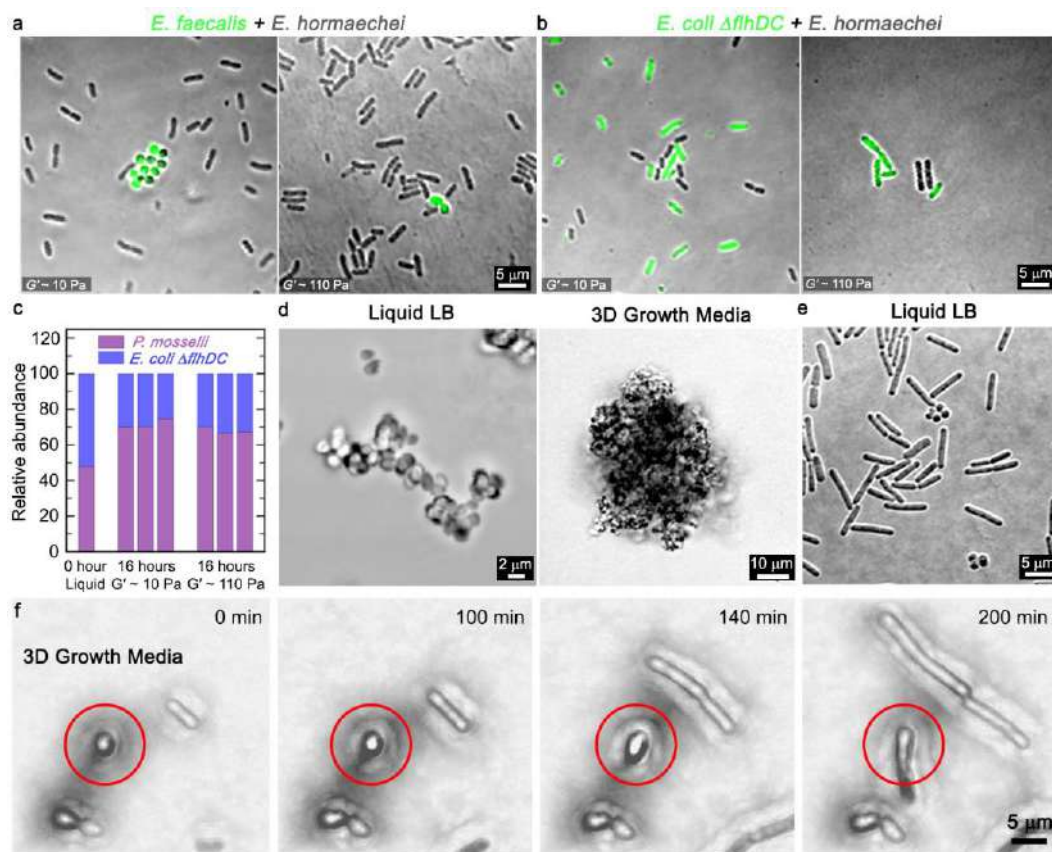


**Figure 12:** (a, b, and c) 3D co-culture models show that high aspect ratio cells (motile *E. hormaechei*) enjoy a distinct advantage over low aspect ratio cells (*E. faecalis*) upon an increase in physical confinement. By contrast, competitive cultures between two different rod-shaped species – *E. coli* and *E. hormaechei*, or, *E. coli* and *P. mosselii* – does not show a significant enrichment of either cell type. (d) *E. faecalis*, which exhibits growth as elongated clusters in liquid LB, instead shows colony growth in the form of spherical colonies in the 3D growth media under physical confinement. (e and f) Growth under confinement leads to dramatically altered outcomes at both the colony and single-cell levels. *P. sanguinis* shows a mixed spherical and rod-shaped morphology in liquid LB, but within microgel growth media, exhibits highly filamentous growth, resulting in elongated colonies.

Thus, we conclude that the aspect ratio of individual cells is a key determinant of the relative biomass ratio under 3D confined growth. To test this, we measure the cell body

1 morphology of all the different bacterial strains used in our experiments and plot their individual  
2 aspect ratio by measuring the major axis and minor axis of the cell body. Distribution of these  
3 aspect ratios captures two different populations, separated by their morphology (**Fig. 10b**).  
4 Superimposing this with our previous results on the relative growth ratios across two different  
5 degrees of confinement, we observe a remarkable compartmentalization of the different  
6 bacterial strains into two non-overlapping domains. This phase space—defined by single-cell  
7 morphology and consequent growth performance under elevated confinement—underscores  
8 the idea that with an increase in confinement, single-cell morphology is the primary  
9 determinant of growth success in complex environments (**Fig. 10c**). Effectively, we  
10 demonstrate that the selective pressure exerted by the physical microenvironment in terms of  
11 confinement-induced spatial constraints strongly favours high aspect ratio cellular morphology  
12 due to its efficient colony organisation.

## 5. Statistical analysis

For each strain of bacteria, we record the OD<sub>600</sub> for a minimum of 4 sets of biological replicates in both low confinement and high confinements matrices. Each set of biological replicates for each type of matrix contains OD<sub>600</sub> data from 2 to 4 technical replicates. For simplicity, consider the data from high confinement to have a mean  $A_{high}$  and standard deviation  $dA_{high}$ , while for low confinement this would be  $A_{low}$  and  $dA_{low}$ , respectively. This can be considered as two random variables  $A_{high}$  and  $A_{low}$ , with errors of  $dA_{high}$  and  $dA_{low}$ , respectively. Now, the relative biomass ratio ( $\rho$ ) can be written as:

$$\rho = A_{high} / A_{low}$$

where  $d\rho$  is the propagated error from the technical replicates of both  $A_{high}$  and  $A_{low}$ . This can be formulated as:

$$d\rho = \sqrt{\left(\left(\frac{\partial \rho}{\partial A_{high}}\right) dA_{high}\right)^2 + \left(\left(\frac{\partial \rho}{\partial A_{low}}\right) dA_{low}\right)^2}$$

Now,  $\frac{\partial \rho}{\partial A_{high}} = \frac{1}{A_{low}}$  and  $\frac{\partial \rho}{\partial A_{low}} = -\frac{A_{high}}{A_{low}^2}$ , hence, we get:

$$d\rho = \sqrt{\left(\left(\frac{1}{A_{low}}\right) dA_{high}\right)^2 + \left(\left(-\frac{A_{high}}{A_{low}^2}\right) dA_{low}\right)^2}$$

Multiplying and dividing R.H.S. by  $\rho$ , we get:

$$d\rho = \rho * \sqrt{\left(\frac{dA_{high}}{A_{high}}\right)^2 + \left(\frac{dA_{low}}{A_{low}}\right)^2}$$

$$\text{Hence, } \rho = A_{high} / A_{low} \pm \rho * \sqrt{\left(\frac{dA_{high}}{A_{high}}\right)^2 + \left(\frac{dA_{low}}{A_{low}}\right)^2}$$

Now, consider the relative biomass ratios of any  $n$  such biological replicates, i.e., some  $\rho_1, \rho_2, \dots \rho_3$ , from  $n$  independent experiments. The average of these will be given by:

$$\rho_{avg} = (\rho_1 + \rho_2 + \dots + \rho_n) / n$$

where,  $d\rho_{avg}$  should represent the propagated error from all the individual relative biomass ratio values. This can be represented as:

$$d\rho_{avg} = \sqrt{\left(\left(\frac{\partial\rho_{avg}}{\partial\rho_1}\right)d\rho_1\right)^2 + \left(\left(\frac{\partial\rho_{avg}}{\partial\rho_2}\right)d\rho_2\right)^2 + \dots + \left(\left(\frac{\partial\rho_{avg}}{\partial\rho_n}\right)d\rho_n\right)^2}$$

Herein, we know that  $\frac{\partial\rho_{avg}}{\partial\rho_1} = \frac{\partial\rho_{avg}}{\partial\rho_2} = \frac{\partial\rho_{avg}}{\partial\rho_n} = \frac{1}{n}$ , which reduces the above to:

$$d\rho_{avg} = \sqrt{(d\rho_1)^2 + (d\rho_2)^2 + \dots + (d\rho_n)^2} / n$$

Hence, the net relative biomass ratio for  $n$  biological replicates, each with its own technical replicates, will be given by:

$$\rho_{avg} = (\rho_1 + \rho_2 + \rho_3 + \dots + \rho_n) / n \pm \sqrt{(d\rho_1)^2 + (d\rho_2)^2 + (d\rho_3)^2 + \dots + (d\rho_n)^2} / n$$

## 6. Discussion and Impact of the Research

Our work provides experimental evidence implying that physical confinement can play a selective role in deciding bacterial growth fitness within their natural niches. High aspect ratio bacteria leverage growth anisotropy to form elongated colonies with higher surface area, allowing better nutrient accessibility as opposed to the spherical colonies formed by low aspect ratio bacteria. Increased confinement strongly selects high aspect ratio cells for more efficient growth — a trend that holds even for high and low aspect ratio forms of the same bacterial strain, indicating a remarkable interconvertible behaviour governed solely by cellular shape. Importantly, we demonstrate the potential to use such constraints to alter bacterial community composition under biomimetic mechanical regimes. Thus, our results represent an important conceptual advancement in how we can experimentally model bacterial growth within complex natural habitats.

In microbial ecology, the present mechanistic understanding of predator-prey interactions, niche partitioning, and community organization largely relies on a framework comprising genetic mutations, behavioural patterns, and biochemical signalling<sup>45–49</sup>. Notably, our platform does not preclude such chemical interactions. Instead, the porous and permeable nature of our 3D matrix presents an opportunity to capture the dynamics of a chemical signalling landscape coupled with different mechanical regimes, enabling a more comprehensive experimental recapitulation of natural niches. While the permeable nature of our 3D matrix allows unimpeded small molecule diffusion, several biological niches such as soil and aquifers resemble semi-permeable porous media with non-deformable, rigid physical barriers. We expect that the reduced nutrient availability and severe spatial restrictions in such contexts significantly restrict colony growth and organization. Recreating such regimes *in vitro* will require the development of semi-permeable 3D scaffolds. Further, within the temporal window of our assays, we do not observe significant contributions from either aberrant phenotypes or perturbed physiologies. However, environmental pressures in the form of nutrient deprivation, high mechanical stiffness, and antagonistic interspecies interactions are known to induce the expression of stress genes, alter metabolism, trigger extreme phenotypes (such as filamentous growth), and favour increased mutational rate<sup>50–55</sup>. Such factors are likely to affect long-term bacterial growth— hence, future work that investigates bacteria under similar conditions over extended durations could provide interesting insights into the long-term effects of confinement on bacterial communities. Presumably, our system can be engineered to recreate such effects by altering the nutrient media composition and tuning the mechanical stiffness of the matrix. We speculate that such environmental constraints will selectively favour a subset of adaptive mutations with the potential to alter evolutionary trajectories. It has been reported that spatial patterning within mixed microbial communities can be strongly driven by single cell morphology<sup>56</sup>. This suggests an interesting direction for future exploration - given the selective pressure enforced by elevated physical confinement favouring rod-shaped bacteria over spherical ones, how do existing spatial patterns get altered when the microenvironmental mechanics change? Conversely, does physical confinement alter the evolution of spatial architecture within mixed microbial communities such as biofilms? Finally, our work highlights the need to explore the role of physical confinement in diverse niches that may select for varied life history strategies. For instance, short-term rapid growth and expansion are not universally preferred traits. In adverse conditions such as in the presence of toxins or predators when long-term cell survival is prioritized, a transient shift towards quiescence or dense collective organisations with minimally exposed surface areas may be

1 more advantageous <sup>57–61</sup>. Such conditions and strategies may override the selection on cell  
2 shape imposed by physical confinement and should be explored further.

3  
4 Current descriptions of microbial growth invoke either genetic mutations or biochemical  
5 signalling as the primary mechanisms via which bacteria respond to their microenvironment.  
6 By contrast, we argue that the spatial constraints imposed by their microenvironment exert a  
7 more general effect, irrespective of specific organismal biology. Our conceptual framework  
8 can be employed to generate coarse-grained predictions of population dynamics under  
9 different biophysical regimes. Understanding how bacteria grow in complex, disordered 3D  
10 environments such as tissues, mucus, and soil, is also central for combating antibiotic  
11 resistance, improving agricultural practices, and bioremediation — underscoring the high-  
12 value practical applications of our work.

## 7. References

1. Leff, J. W. *et al.* Consistent responses of soil microbial communities to elevated nutrient inputs in grasslands across the globe. *Proc Natl Acad Sci U S A* **112**, 10967–10972 (2015).
2. Estrela, S., Sanchez-Gorostiaga, A., Vila, J. C. C. & Sanchez, A. Nutrient dominance governs the assembly of microbial communities in mixed nutrient environments. *Elife* **10**, (2021).
3. Keegstra, J. M., Carrara, F. & Stocker, R. The ecological roles of bacterial chemotaxis. *Nature Reviews Microbiology* **20**, 491–504 (2022).
4. Gonzalez, D. & Mavridou, D. A. I. Making the Best of Aggression: The Many Dimensions of Bacterial Toxin Regulation. *Trends Microbiol* **27**, 897–905 (2019).
5. Blasche, S. *et al.* Metabolic cooperation and spatiotemporal niche partitioning in a kefir microbial community. *Nature Microbiology* **6**, 196–208 (2021).
6. Chang, C. Y., Bajić, D., Vila, J. C. C., Estrela, S. & Sanchez, A. Emergent coexistence in multispecies microbial communities. *Science* (1979) **381**, 343–348 (2023).
7. Persat, A. *et al.* The Mechanical World of Bacteria. *Cell* **161**, 988 (2015).
8. Datta, S. S., Steinberg, A. P. & Ismagilova, R. F. Polymers in the gut compress the colonic mucus hydrogel. *Proc Natl Acad Sci U S A* **113**, 7041–7046 (2016).
9. Ribet, D. & Cossart, P. How bacterial pathogens colonize their hosts and invade deeper tissues. *Microbes Infect* **17**, 173–183 (2015).
10. Gomez, S. *et al.* Substrate stiffness impacts early biofilm formation by modulating *Pseudomonas aeruginosa* twitching motility. *Elife* **12**, (2023).
11. Tchoufag, J., Ghosh, P., Pogue, C. B., Nan, B. & Mandadapu, K. K. Mechanisms for bacterial gliding motility on soft substrates. *Proc Natl Acad Sci U S A* **116**, 25087–25096 (2019).
12. Flemming, H. C. *et al.* Biofilms: an emergent form of bacterial life. *Nature Reviews Microbiology* **14**, 563–575 (2016).
13. Schloss, P. D. & Handelsman, J. Toward a Census of Bacteria in Soil. *PLoS Comput Biol* **2**, e92 (2006).
14. Fan, Y. & Pedersen, O. Gut microbiota in human metabolic health and disease. *Nature Reviews Microbiology* **19**, 55–71 (2020).
15. Nicholson, P. G. *Soil Improvement and Ground Modification Methods*. *Soil Improvement and Ground Modification Methods* (2015).
16. Lu, P., Takai, K., Weaver, V. M. & Werb, Z. Extracellular matrix degradation and remodeling in development and disease. *Cold Spring Harb Perspect Biol* **3**, (2011).
17. Belkaid, Y. & Hand, T. W. Role of the microbiota in immunity and inflammation. *Cell* **157**, 121–141 (2014).
18. Kreda, S. M., Davis, C. W. & Rose, M. C. CFTR, Mucins, and Mucus Obstruction in Cystic Fibrosis. *Cold Spring Harb Perspect Med* **2**, a009589 (2012).
19. Shao, X. *et al.* Growth of bacteria in 3-d colonies. *PLoS Comput Biol* **13**, e1005679 (2017).
20. Martinez-Calvo, A. *et al.* Morphological instability and roughening of growing 3D bacterial colonies. *Proc Natl Acad Sci U S A* **119**, e2208019119 (2022).
21. Kannan, H. *et al.* Spatiotemporal development of growth and death zones in expanding bacterial colonies driven by emergent nutrient dynamics. *bioRxiv* 2023.08.27.554977 (2023) doi:10.1101/2023.08.27.554977.

- 1 22. Dell'Arciprete, D. *et al.* A growing bacterial colony in two dimensions as an active  
2 nematic. *Nature Communications* 2018 9:1 **9**, 1–9 (2018).
- 3 23. You, Z., Pearce, D. J. G., Sengupta, A. & Giomi, L. Mono-to Multilayer Transition in  
4 Growing Bacterial Colonies. *Phys Rev Lett* **123**, 178001 (2019).
- 5 24. Bhattacharjee, T. & Datta, S. S. Bacterial hopping and trapping in porous media.  
6 *Nature Communications* 2019 10:1 **10**, 1–9 (2019).
- 7 25. Lai, S. K., Wang, Y. Y., Hida, K., Cone, R. & Hanes, J. Nanoparticles reveal that  
8 human cervicovaginal mucus is riddled with pores larger than viruses. *Proc Natl Acad*  
9 *Sci U S A* **107**, 598–603 (2010).
- 10 26. Sardelli, L. *et al.* Towards bioinspired in vitro models of intestinal mucus. *RSC Adv* **9**,  
11 15887–15899 (2019).
- 12 27. Bhattacharjee, T. & Datta, S. S. Confinement and activity regulate bacterial motion in  
13 porous media. *Soft Matter* **15**, 9920–9930 (2019).
- 14 28. Bhattacharjee, T. *et al.* Polyelectrolyte scaling laws for microgel yielding near  
15 jamming. *Soft Matter* **14**, 1559–1570 (2018).
- 16 29. Bhattacharjee, T. *et al.* Liquid-like Solids Support Cells in 3D. *ACS Biomater Sci Eng*  
17 **2**, 1787–1795 (2016).
- 18 30. Sleator, R. D. & Hill, C. Bacterial osmoadaptation: the role of osmolytes in bacterial  
19 stress and virulence. *FEMS Microbiol Rev* **26**, 49–71 (2002).
- 20 31. Wood, J. M. Bacterial responses to osmotic challenges. *Journal of General*  
21 *Physiology* **145**, 381–388 (2015).
- 22 32. Osawa, M. & Erickson, H. P. Turgor pressure and possible constriction mechanisms  
23 in bacterial division. *Front Microbiol* **9**, 331686 (2018).
- 24 33. Kamashev, D., Balandina, A. & Rouviere-Yaniv, J. The binding motif recognized by  
25 HU on both nicked and cruciform DNA. *EMBO J* **18**, 5434–5444 (1999).
- 26 34. Burby, P. E. & Simmons, L. A. Regulation of cell division in bacteria by monitoring  
27 genome integrity and DNA replication status. *J Bacteriol* **202**, (2020).
- 28 35. Rudge, T. J., Steiner, P. J., Phillips, A. & Haseloff, J. Computational Modeling of  
29 Synthetic Microbial Biofilms. *ACS Synth Biol* **1**, 345–352 (2012).
- 30 36. Pinho, M. G., Kjos, M. & Veening, J. W. How to get (a)round: mechanisms controlling  
31 growth and division of coccoid bacteria. *Nature Reviews Microbiology* 2013 11:9 **11**,  
32 601–614 (2013).
- 33 37. Bean, G. J. *et al.* A22 disrupts the bacterial actin cytoskeleton by directly binding and  
34 inducing a low-affinity state in MreB. *Biochemistry* **48**, 4852–4857 (2009).
- 35 38. Khandige, S. *et al.* DamX controls reversible cell morphology switching in  
36 uropathogenic escherichia coli. *mBio* **7**, 642–658 (2016).
- 37 39. Lee, Y. & Wang, C. Morphological Change and Decreasing Transfer Rate of Biofilm-  
38 Featured *Listeria monocytogenes* EGDe. *J Food Prot* **80**, 368–375 (2017).
- 39 40. Espinosa, E. *et al.* l-Arabinose Induces the Formation of Viable Nonproliferating  
40 Spheroplasts in *Vibrio cholerae*. *Appl Environ Microbiol* **87**, 1–15 (2021).
- 41 41. Khandige, S. *et al.* DamX Controls Reversible Cell Morphology Switching in  
42 Uropathogenic *Escherichia coli*. *mBio* **7**, (2016).
- 43 42. Bockwoldt, J. A., Zimmermann, M., Tiso, T. & Blank, L. M. Complete Genome  
44 Sequence and Annotation of the *Paracoccus pantotrophus* Type Strain DSM 2944.  
45 *Microbiol Resour Announc* **9**, (2020).
- 46 43. McGinnis, J. M. *et al.* *Paracoccus sanguinis* sp. nov., isolated from clinical specimens  
47 of New York state patients. *Int J Syst Evol Microbiol* **65**, 1877–1882 (2015).



- 1 44. Nokhal, T. H. & Mayer, F. Structural analysis of four strains of *Paracoccus*  
2 *denitrificans*. *Antonie Van Leeuwenhoek* **45**, 185–197 (1979).
- 3 45. Quinn, R. A. *et al.* Niche partitioning of a pathogenic microbiome driven by chemical  
4 gradients. *Sci Adv* **4**, (2018).
- 5 46. Baran, R. *et al.* Exometabolite niche partitioning among sympatric soil bacteria.  
6 *Nature Communications* 2015 6:1 **6**, 1–9 (2015).
- 7 47. Brochet, S. *et al.* Niche partitioning facilitates coexistence of closely related gut  
8 bacteria. *Elife* **10**, (2021).
- 9 48. Nair, R. R. *et al.* Bacterial predator-prey coevolution accelerates genome evolution  
10 and selects on virulence-associated prey defences. *Nature Communications* 2019  
11 10:1 **10**, 1–10 (2019).
- 12 49. Wongkiew, S., Chaikaew, P., Takrattanasaran, N. & Khamkajorn, T. Evaluation of  
13 nutrient characteristics and bacterial community in agricultural soil groups for  
14 sustainable land management. *Scientific Reports* 2022 12:1 **12**, 1–13 (2022).
- 15 50. Battesti, A., Majdalani, N. & Gottesman, S. The RpoS-mediated general stress  
16 response in *Escherichia coli* \*. *Annu Rev Microbiol* **65**, 189–213 (2011).
- 17 51. Benomar, S. *et al.* Nutritional stress induces exchange of cell material and energetic  
18 coupling between bacterial species. *Nature Communications* 2015 6:1 **6**, 1–10 (2015).
- 19 52. Peterson, S. B., Bertolli, S. K. & Mougous, J. D. Interbacterial antagonism: at the  
20 center of bacterial life. *Curr Biol* **30**, R1203 (2020).
- 21 53. MacLean, R. C., Torres-Barceló, C. & Moxon, R. Evaluating evolutionary models of  
22 stress-induced mutagenesis in bacteria. *Nature Reviews Genetics* 2013 14:3 **14**, 221–  
23 227 (2013).
- 24 54. Foster, P. L. Stress-Induced Mutagenesis in Bacteria. *Crit Rev Biochem Mol Biol* **42**,  
25 373 (2007).
- 26 55. Tran, T. D., Ali, M. A., Lee, D., Félix, M. A. & Luallen, R. J. Bacterial filamentation as a  
27 mechanism for cell-to-cell spread within an animal host. *Nature Communications* 2022  
28 13:1 **13**, 1–11 (2022).
- 29 56. Smith, W. P. J. *et al.* Cell morphology drives spatial patterning in microbial  
30 communities. *Proc Natl Acad Sci U S A* **114**, E280–E286 (2017).
- 31 57. Monier, J. M. & Lindow, S. E. Differential survival of solitary and aggregated bacterial  
32 cells promotes aggregate formation on leaf surfaces. *Proc Natl Acad Sci U S A* **100**,  
33 15977–15982 (2003).
- 34 58. Rutherford, S. T. & Bassler, B. L. Bacterial Quorum Sensing: Its Role in Virulence and  
35 Possibilities for Its Control. *Cold Spring Harb Perspect Med* **2**, (2012).
- 36 59. Li, S., Liu, S. Y., Chan, S. Y. & Chua, S. L. Biofilm matrix cloaks bacterial quorum  
37 sensing chemoattractants from predator detection. *ISME J* **16**, 1388 (2022).
- 38 60. Matz, C. *et al.* Marine Biofilm Bacteria Evade Eukaryotic Predation by Targeted  
39 Chemical Defense. *PLoS One* **3**, 2744 (2008).
- 40 61. Gray, D. A. *et al.* Extreme slow growth as alternative strategy to survive deep  
41 starvation in bacteria. *Nature Communications* 2019 10:1 **10**, 1–12 (2019).
- 42 62. Crocker, J. C. & Grier, D. G. Methods of Digital Video Microscopy for Colloidal  
43 Studies. *J Colloid Interface Sci* **179**, 298–310 (1996).
- 44 63. Naik, T., Sharda, M., Lakshminarayanan, C. P., Virbhadr, K. & Pandit, A. High-  
45 quality single amplicon sequencing method for illumina MiSeq platform using pool of  
46 'N' (0-10) spacer-linked target specific primers without PhiX spike-in. *BMC Genomics*  
47 **24**, (2023).

1 64. Callahan, B. J. *et al.* DADA2: High-resolution sample inference from Illumina amplicon  
2 data. *Nature Methods* 2016 13:7 **13**, 581–583 (2016).  
3  
4



Signed:  
Sreepadmanabh M  
30-08-24  
NCBS-TIFR